J. Fluid Mech. (2000), *vol.* 420, *pp.* 85–130. Printed in the United Kingdom

Modes of vortex formation and frequency response of a freely vibrating cylinder

By R. GOVARDHAN AND C. H. K. WILLIAMSON

Sibley School of Mechanical and Aerospace Engineering, Upson Hall, Cornell University, Ithaca, NY 14853-7501, USA

(Received 22 December 1999 and in revised form 21 April 2000)

In this paper, we study the transverse vortex-induced vibrations of an elastically mounted rigid cylinder in a fluid flow. We use simultaneous force, displacement and vorticity measurements (using DPIV) for the first time in free vibrations. There exist two distinct types of response in such systems, depending on whether one has a high or low combined mass–damping parameter ($m^*\zeta$). In the classical high-($m^*\zeta$) case, an 'initial' and 'lower' amplitude branch are separated by a discontinuous mode transition, whereas in the case of low ($m^*\zeta$), a further higher-amplitude 'upper' branch of response appears, and there exist two mode transitions.

To understand the existence of more than one mode transition for low ($m^*\zeta$), we employ two distinct formulations of the equation of motion, one of which uses the 'total force', while the other uses the 'vortex force', which is related only to the dynamics of vorticity. The first mode transition involves a jump in 'vortex phase' (between vortex force and displacement), ϕ_{vortex}, at which point the frequency of oscillation (f) passes through the natural frequency of the system in the fluid, $f \sim f_{Nwater}$. This transition is associated with a jump between 2S $\leftrightarrow$ 2P vortex wake modes, and a corresponding switch in vortex shedding timing. Across the second mode transition, there is a jump in 'total phase', ϕ_{total}, at which point $f \sim f_{Nvacuum}$. In this case, there is no jump in ϕ_{vortex}, since both branches are associated with the 2P mode, and there is therefore no switch in timing of shedding, contrary to previous assumptions. Interestingly, for the high-($m^*\zeta$) case, the vibration frequency jumps across both f_{Nwater} and $f_{Nvacuum}$, corresponding to the simultaneous jumps in ϕ_{vortex} and ϕ_{total}. This causes a switch in the timing of shedding, coincident with the 'total phase' jump, in agreement with previous assumptions.

For large mass ratios, $m^* = O(100)$, the vibration frequency for synchronization lies close to the natural frequency ($f^* = f/f_N \approx 1.0$), but as mass is reduced to $m^* = O(1)$, f^* can reach remarkably large values. We deduce an expression for the frequency of the lower-branch vibration, as follows:

$$f^*_{lower} = \sqrt{\frac{(m^* + C_A)}{(m^* - 0.54)}},$$

which agrees very well with a wide set of experimental data. This frequency equation uncovers the existence of a *critical mass ratio*, where the frequency f^* becomes large: $m^*_{crit} = 0.54$. When $m^* < m^*_{crit}$, the lower branch can never be reached and it ceases to exist. The upper-branch large-amplitude vibrations persist for all velocities, no matter how high, and the frequency increases indefinitely with flow velocity. Experiments at $m^* < m^*_{crit}$ show that the upper-branch vibrations continue to the limits (in flow speed) of our facility.

1. Introduction and preliminary work

The problem of vortex-induced vibration of structures is important in many fields of engineering. It is a cause for concern in the dynamics of riser tubes bringing oil from the seabed to the surface, in flow around heat exchanger tubes, in the dynamics of civil engineering structures such as bridges and chimneys, and also in many other situations of practical importance. The wide range of problems caused by vortex-induced vibration has led to a large number of fundamental studies, which are summarized in the comprehensive reviews of Sarpkaya (1979), Griffin & Ramberg (1982), Bearman (1984), Parkinson (1989), and in the books by Blevins (1990), Naudascher & Rockwell (1994), and Sumer & Fredsøe (1997). In the present work, we are interested in one of the most conceptually simple situations of such fluid–structure interaction: the case of an elastically mounted rigid cylinder constrained to move transversely to a uniform free stream. There has been a great deal of interest recently in investigating experimental conditions of low mass and damping. Such results are at present being compared with both the classical high-mass experiments, and with direct numerical simulations (DNS) of this flow. Related studies on flexible cylindrical cantilevers (for example, Vickery & Watkins 1964; Fujarra *et al.* 1998; Pesce & Fujarra 2000), on cylinders in a shear flow (Stansby 1976; Griffin 1985; Balasubramanian & Skop 1996) and on numerical simulations of long flexible cables (Newman & Karniadakis 1997; Evangelinos & Karniadakis 1999), have also received renewed attention, fuelled in part by the present interest in the dynamics of offshore structures.

In the conceptually simple case of the elastically mounted rigid cylinder, there are a number of fundamental unanswered questions, some of which were recently outlined by Khalak & Williamson (1999). Related to their points, we raise here the following questions, as part of the 'driving force' for the present work:

- What modes of response exist and what are their corresponding wake vortex dynamics?
- We seek to understand the well-known 'phase-jump' (a jump in the phase between transverse force and cylinder displacement) that occurs in the synchronization region. Following the work of Khalak & Williamson (1996, 1997, 1999), we ask the question: Why can there exist *two separate mode jumps* at sufficiently low mass and damping?
- What is the effect of mass ratio on the frequency response and on the range of synchronization?

Before addressing the above points, we shall briefly introduce an equation of motion generally used to represent the vortex-induced vibrations of a cylinder in the transverse y-direction (perpendicular to the free stream), as follows:

$$m\ddot{y} + c\dot{y} + ky = F, \tag{1.1}$$

where m is the total oscillating structural mass (i.e. not including added mass); c is the structural damping; k is the spring constant; and F is the fluid force in the transverse direction. When the body oscillation frequency is synchronized with the periodic vortex wake mode, good approximations to the force, $F(t)$, and the response displacement $y(t)$, are given by

$$F(t) = F_o \sin(\omega t + \phi), \tag{1.2}$$

$$y(t) = A \sin(\omega t), \tag{1.3}$$

where $\omega = 2\pi f$; f is the oscillation frequency. The phase angle ϕ, between the fluid force and the body displacement, is crucial in determining the energy transfer from the

fluid to the body, and hence in influencing the amplitude of oscillation, as pointed out clearly in the previous review papers (e.g. Sarpkaya 1979; Bearman 1984). We select a set of relevant non-dimensional parameters in this problem, which are presented in table 1.

The response amplitude and frequency may be derived in a straightforward manner from equations (1.1)–(1.3), and are formulated here, along the lines of Khalak & Williamson (1999), as follows:

$$A^* = \frac{1}{4\pi^3}\frac{C_Y \sin\phi}{(m^* + C_A)\zeta}\left(\frac{U^*}{f^*}\right)^2 f^*, \tag{1.4}$$

$$f^* = \sqrt{\frac{(m^* + C_A)}{(m^* + C_{EA})}}, \tag{1.5}$$

where C_A is the potential flow added-mass coefficient ($C_A = 1.0$ for a circular cylinder), and C_{EA} is an 'effective' added-mass coefficient that includes an apparent effect due to the total transverse fluid force in phase with the body acceleration ($C_Y \cos\phi$):

$$C_{EA} = \frac{1}{2\pi^3 A^*}\left(\frac{U^*}{f^*}\right)^2 C_Y \cos\phi. \tag{1.6}$$

A fundamental question, regarding such an elastically mounted system, is how the peak response amplitude (A^*_{max}) will vary as a function of $\{m^*, \zeta\}$, where ζ is the damping ratio. Much discussion on this point, concerning especially the most recent work, is reviewed in the 'Review and preliminary results' section of Khalak & Williamson (1999), and only a brief outline of this point will be presented here. Generally, in the literature, A^*_{max} has been plotted versus a parameter, S_G, which is proportional to the product of mass and damping, and is defined as

$$S_G = 2\pi^3 S^2(m^*\zeta), \tag{1.7}$$

where S is the Strouhal number for the static cylinder. This 'Skop–Griffin' parameter (S_G) was used in the first comprehensive compilation and plot of existing peak amplitude (A^*_{max}) data as a function of S_G, by Griffin and co-workers in the 1970s (see Griffin, Skop & Ramberg 1975), and we define such a plot here as a 'Griffin' plot. The logic in choosing a combined mass–damping parameter, like S_G, comes from observation of equation (1.4) for A^*, and has been discussed in many previous papers. Bearman (1984), for example, discusses in his review that for large mass ratio ($m^* \gg 1$), the actual cylinder oscillation frequency (f) at resonance will be close to the vortex shedding frequency for a static cylinder (f_{vo}), and also close to the system natural frequency (f_N), i.e. $f \approx f_{vo} \approx f_N$ and thus $f^* = f/f_N \approx 1.0$. One may also note that for large m^*, in equation (1.5) and with C_A, $C_{EA} = O(1)$, $f^* \approx 1.0$. Hence, at resonance, the parameter $(U^*/f^*) = (U/fD) \approx (U/f_{vo}D) = 1/S$, which is thus close to 5.0. The assumption is therefore often made that both (U^*/f^*) and f^* are constants, under resonance conditions, giving

$$A^*_{max} \propto \frac{C_Y \sin\phi}{(m^* + C_A)\zeta}. \tag{1.8}$$

Under these assumptions, A^*_{max} is a function of the product of mass and damping $(m^* + C_A)\zeta$. Concerns over the use of such a combined mass–damping parameter at low mass ratios have been clearly discussed by Sarpkaya (1978, 1979) and by Zdravkovich (1990). However, the recent results of Khalak & Williamson (1999),

Mass ratio	m^*	$\dfrac{m}{\pi\rho D^2 L/4}$
Damping ratio	ζ	$\dfrac{c}{2\sqrt{k(m+m_A)}}$
Velocity ratio	U^*	$\dfrac{U}{f_N D}$
Amplitude ratio	A^*	$\dfrac{A}{D}$
Frequency ratio	f^*	$\dfrac{f}{f_N}$
Transverse force coefficient	C_Y	$\dfrac{F}{\frac{1}{2}\rho U^2 DL}$
Reynolds number	Re	$\dfrac{\rho UD}{\mu}$

TABLE 1. Non-dimensional groups. In this paper, in places where f^* is defined without a subscript, it is taken to be the frequency ratio (f/f_N), where f is the oscillation frequency, and f_N is the natural frequency in water. The added mass, m_A, is given by $m_A = C_A m_d$, where m_d is the displaced fluid mass and C_A is the potential added-mass coefficient. ($C_A = 1.0$ for a circular cylinder). In the above groups, D = cylinder diameter, L = cylinder length, ρ = fluid density, U = free-stream velocity, μ = viscosity.

show that even for low m^* of the order of 2 and very low mass–damping down to the value $(m^* + C_A)\zeta \sim 0.006$, the use of a single combined mass–damping parameter collapses peak amplitude data very well, even for a wide independent variation of parameters m^* and ζ.

There exist two types of response character for such an elastically mounted system, depending on whether the combined mass–damping parameter ($m^*\zeta$) is high, or whether ($m^*\zeta$) is low, as pointed out by Khalak & Williamson (1999). A well-known study of the response of an elastically mounted cylinder at high $(m^*\zeta) \sim 0.25$ was conducted by Feng (1968). As shown schematically in figure 1(*a*), he observed two different branches of amplitude response, which we describe as an 'initial' branch, corresponding to the highest amplitudes reached, and a 'lower' branch. Subsequent experiments at high ($m^*\zeta$) on a vibrating cable (Brika & Laneville 1993) also demonstrate two such branches of response. It should be noted here, that in both of these experiments hysteresis was observed in the transition between the two branches, denoted by H in figure 1(*a*). In contrast to the cases above, the low-($m^*\zeta$) experiments of Khalak & Williamson (1996, 1997, 1999) show the existence of three different branches of response. In addition to the 'initial' and 'lower' branches, they also find an 'upper' branch of response, as shown schematically in figure 1(*b*), and thereby find two mode transitions. They found the transition between 'initial' and 'upper' branch to be hysteretic, while the transition from 'upper' to 'lower' branch involved an intermittent switching of modes.

Maximum amplitude (A^*_{max}) is plotted versus a combined mass–damping parameter, $(m^* + C_A)\zeta$, in figure 2, using data from several investigators, in what we call a 'Griffin' plot. The set of data marked 'upper' corresponds with 'upper'-branch peak amplitudes, while the data denoted by 'lower' are for 'lower'-branch peak amplitudes. The solid line represents a curve fit to the data of a large number of investigators, and includes

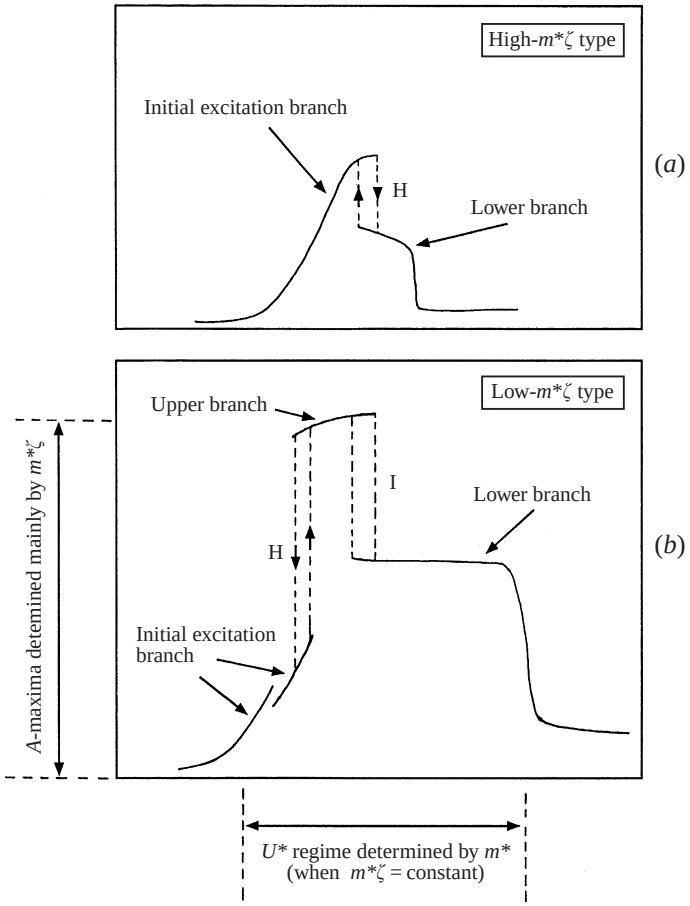

FIGURE 1. The two distinct types of amplitude response are shown here schematically. (Vertical axes represent A^* and horizontal axes represent U^*.) The Feng-type of high-($m^*\zeta$) response exhibits only two branches (initial and lower), while the low-($m^*\zeta$) type of response (Khalak & Williamson 1999) exhibits three branches (initial, upper and lower). The mode transitions are either hysteretic (H) or involve intermittent switching (I). The range of synchronization is controlled primarily by m^* (when $m^*\zeta$ is constant), whereas the peak amplitudes are controlled principally by the product of $m^*\zeta$.

a collection of some quite different types of experiments, compiled originally by Griffin (1980), and updated recently by Skop & Balasubramanian (1997). The curve fit has classically been used to represent not only oscillations of rigid cylinders but also flexible cantilevers and pivoted cylinders. However, the recent data of Khalak & Williamson (1999), and of Hover, Techet & Triantafyllou (1998), for strictly elastically mounted rigid cylinders depart substantially from the curve fit. It is also of interest that the maximum response ($A^*_{max} \approx 0.6$) coming from DNS of this flow at low Reynolds numbers ($Re \sim 200$) is markedly lower than the data for high Reynolds number experiments. We believe that this large difference in response amplitude is a Reynolds number effect, since the experimental amplitudes in Anagnostopoulos & Bearman (1992), also at low $Re \approx 90$–150, exhibit a similar maximum response ($A^*_{max} \approx 0.55$) to the DNS computations. The bull's eye symbols in figure 2 correspond to the present experiments, one pair being for the low-($m^*\zeta$) type of response, and the other for the high-($m^*\zeta$) type of response. A comprehensive study of the amplitudes,

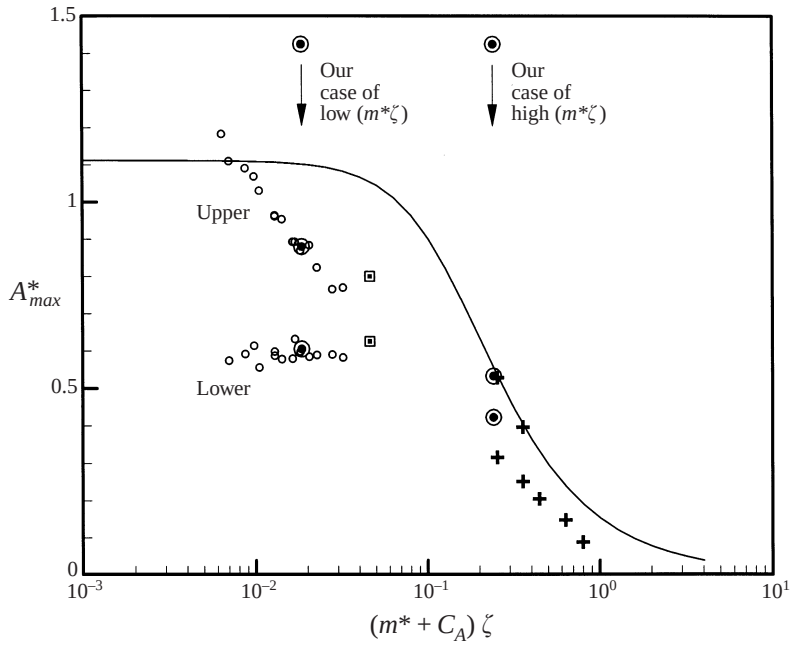

FIGURE 2. 'Griffin' plot showing peak amplitude A^*_{max} versus a combined mass–damping parameter $[(m^* + C_A)\zeta]$. The 'bull's eye' symbols (⊙) indicate the cases studied in detail in this paper. +, Feng (1968); ⊡, Hover *et al.* (1998); ○, Khalak & Williamson (1999); ——, Skop & Balasubramanian (1997).

forces, vortex dynamics and mode jumps of these two distinct types of response forms the basis of this paper.

An important feature of the dynamics of such elastically mounted systems is the jump in phase (ϕ), between the transverse force (C_Y) and the cylinder displacement (y), that occurs when the response changes modes, as in figure 1(a). A number of forced-vibration studies (for example, Bishop & Hassan 1964; Stansby 1976; Bearman & Currie 1979; Gopalkrishnan 1993) have also shown either a jump or a sharp change in phase, in the central part of the synchronization regime (as defined by the range of U^* over which synchronization takes place). Zdravkovich (1982) first showed, by observing flow-visualization from previous studies, that this phase jump was connected to a switch in the timing of vortex shedding, and this has since been confirmed from forced vibration by Gu, Chyu & Rockwell (1994) at low amplitude ($A^* = 0.2$), and from the numerical simulations of Lu & Dalton (1996). From recent two-dimensional simulations at $Re = 500$, Blackburn & Henderson (1999), put forward the idea that this switch in timing is caused by a competition between two different mechanisms of vorticity production.

A number of investigators also report a change in the pattern of vortex formation, as one varies normalized velocity U^* or amplitude A^*. Griffin & Ramberg (1974) first showed, for large-amplitude forced-vibration experiments (at low $Re \approx 190$), that an asymmetric mode occurred whereby three vortices were formed per cycle. Subsequent forced-vibration studies by Williamson & Roshko (1988), over a wide range of A^* and U^* (at $Re = 300$–1000), show a number of different vortex formation modes, which are defined, for example, as '2S' indicating 2 single vortices formed per cycle, '2P' meaning 2 pairs of vortices formed per cycle and a 'P+S' mode comprising a

pair of vortices and a single vortex per cycle, like the asymmetric mode observed in Griffin & Ramberg (1974). They suggested that the phase jump corresponds with a change of mode from '2S' to '2P'. Ongoren & Rockwell (1988) found in the case of *streamwise* vibrations at very low amplitudes ($A^* \approx 0.13$), an equivalent pattern to the '2P' mode.

Digital particle image velocimetry (DPIV) measurements by Sheridan *et al.* (1998) confirm the existence of the 2P mode in forced transverse vibrations. Fascinating wake dynamics have been found by Techet, Hover & Triantafyllou (1998), in the case of the forced vibrations of a tapered cylinder, where a 'hybrid' mode was found to comprise the 2P and 2S modes occurring simultaneously at different spanwise locations along the cylinder. Interestingly, a number of accurate two-dimensional numerical simulations, at low $Re \sim 200$ (for example, Meneghini & Bearman 1995; Blackburn & Henderson 1995), and at $Re = 500$ (Blackburn & Henderson 1999), as well as some experiments (Jeon, Shan & Gharib 1995; Atsavapranee *et al.* 1998), clearly do not find the 2P mode. Evangelinos & Karniadakis (1999) have recently conducted simulations at $Re = 1000$. In agreement with our experiments, they find vortex deformations and multiple vorticity concentrations in the near wake. However, interestingly, they find transient mixtures of (P+S) and 2P modes in the near wake, with possible formation of a 2S mode, or 'general wake instability', as the flow travels downstream. They conclude that their simulations indicate 'the (P+S) pattern may also be associated with the upper branch'. There has thus been some debate as to the existence of the 2P mode as a steady-state pattern. In the present paper, we shall show results from DPIV and response measurements which confirm the existence of a steady-state 2P mode. In other words, this is not a transient mode, as suggested by the results in some previous studies, and it is found to be a remarkably periodic mode which occurs for indefinite time.

Brika & Laneville (1993) and Khalak & Williamson (1999) both show from flow-visualizations in free vibration that the jump from the initial branch to the lower branch corresponds with a mode change from 2S to 2P, as proposed in the forced vibration studies of Williamson & Roshko (1988). The ingenious virtual free vibration experiments by Hover *et al.* (1998) yield a complete response plot which corresponds well with the map of vortex modes from Williamson & Roshko (1988), again suggesting that the initial branch is the 2S mode, and the lower branch is the 2P mode. The flow visualizations mentioned earlier are indicative of the 2S and 2P modes, but at high $Re \sim 5000$, the technique is somewhat unclear. As regards the upper branch, the flow visualization in Khalak & Williamson (1999) was not of sufficient resolution to determine categorically the existing wake vortex mode. We shall set out, in this paper, to provide clear evidence of the vortex formation modes corresponding, not only to the initial and lower branches, but also to the upper branch, by the use of the digital particle image velocimetry (DPIV) technique, to determine velocity and vorticity fields in the wake.

Another important feature of these systems is 'synchronization' or 'lock-in', the definition of which has led to some recent discussions in the literature. Typically this phenomenon is described as involving a synchronization of the vortex formation frequency (f_v), and the body oscillation frequency (f) with the natural frequency (f_N), such that $f^* = f/f_N$ is close to unity, over a range of velocity, U^* (see Blevins 1990 and Sumer & Fredsøe 1997). This classic scenario is approximately valid for large $m^* = O(100)$. However, at the low mass ratios typically found for a structure vibrating in water $m^* = O(10)$, Moe & Wu (1990), Khalak & Williamson (1997) and Gharib *et al.* (1998) observe a marked departure of f^* from unity during 'lock-in'.

In fact, Khalak & Williamson (1997) find values of $f^* \approx 1.4$ during synchronization. However, one should expect to find such a departure of f^* from unity, based on the discussion of Bearman (1984), and based on the 'added mass coefficient' data of Sarpkaya (1978). We cannot thus define lock-in or synchronization such that the shedding frequency is necessarily close to the natural frequency. Khalak & Williamson (1999) hence suggested a more suitable definition of synchronization as the matching of the frequency of the periodic wake vortex mode with the body oscillation frequency. Correspondingly, the fluid force frequency must match the shedding frequency, which is the useful definition of lock-in used by Sarpkaya (1995).

The widening of the synchronization regime (as measured by a range of U^*) is another important effect of low m^*, and was first seen in the experiments of Ramberg & Griffin (1981). The recent experiments of Khalak & Williamson (1999), where the mass–damping ($m^*\zeta$) was maintained at a very low value, show a significant increase in the regime of synchronization, relative to Feng's (1968) original work. However, by using the actual oscillation frequency (f) rather than the still-water natural frequency (f_N) to form a normalized velocity, i.e. by using $(U^*/f^*) = (U/fD)$, rather than simply U^*, they were able to obtain a good collapse of a set of response plots, for a wide range of m^*. The collapsed amplitude response branches were also found to match well the Williamson & Roshko (1988) map of vortex wake patterns from forced vibration studies. A 'true' reduced velocity, similar to U^*/f^*, has been used by Moe & Wu (1990) and Hover *et al.* (1998) to compare free-vibration results with forced-vibration experiments, and an equivalent parameter ($Vr\,St$) was used by Sarpkaya (1995).

In summary, the case of an oscillating body in water is associated with relatively small mass ratios, $m^* = O(10)$, which leads to an increase of synchronized oscillation frequency $f^* > 1.0$, and to an increase in the regime of synchronization. However, in this paper we would like to predict the levels of f^* through this regime, as a function of these low mass ratios, m^*. We shall present simple quantitative predictions of both oscillation frequency and regime of synchronization.

Following a description of the experimental methods in the next section (§ 2), we shall present a set of amplitude and frequency plots, and force measurements, corresponding to two distinct cases: first (in § 3), the case of low ($m^*\zeta$) comprising the initial–upper–lower response branches; and secondly (in § 4), the case of high ($m^*\zeta$) comprising only the initial–lower branches. We shall introduce the concept of using two distinct phases to characterize the fluid–structure interaction. At high ($m^*\zeta$), the classical phase, ϕ, between the total fluid force and displacement exhibits a jump during the transition between initial and lower branches, as is well known. However, at low ($m^*\zeta$), we have three principal response branches, and therefore two mode transitions. By introducing a 'vortex phase', ϕ_{vortex}, defined as the phase angle between the 'vortex force' and displacement, we show that the initial $\leftrightarrow$ upper transition is associated with a jump in vortex phase ϕ_{vortex}, which then corresponds with a switch in the timing of vortex shedding. This is quite distinct from the jump in ϕ, which occurs at the upper–lower transition, and where there is no distinct switch in timing of vortex shedding. *The classical assumption that the phase (ϕ) jump is necessarily associated with a jump change in the timing of vortex formation is therefore not correct for low mass–damping.*

The modes of vortex formation for each of the three branches at low ($m^*\zeta$), and for the two branches present at high ($m^*\zeta$), are shown clearly from DPIV, in § 5. In § 6, we shall examine the effect of mass ratio m^* on the frequency response f^* during synchronization. We shall obtain a simple equation which accurately predicts the

frequency f^* in the lower branch, for small mass ratios m^*, and which will uncover the existence of a *critical mass ratio* m^*_{crit} below which the regime of synchronization becomes infinitely large. Following this, we present conclusions in § 7.

2. Experimental details

The present experiments were conducted using a hydroelastic facility, which is described in detail in Khalak & Williamson (1996, 1999), in conjunction with the Cornell-ONR Water Channel. The hydroelastic facility comprises air bearings mounted above the channel test section, which allow a vertical cylinder in the fluid to move transverse to the free stream. The turbulence level in the test section of the water channel was less than 0.9%, in the 15 in. × 20 in. (0.381 m × 0.508 m) cross-section, over the range of free-stream velocities U (0.04–0.32 m s^{-1}) used in this study. Cylinders of diameter 0.0381 m and 0.0127 m were used for the low mass–damping and high mass–damping cases, respectively. The corresponding length–diameter ratio was 10 and 20, respectively. The mass ratio was varied by adding mass to the oscillating structure above the water channel. In all the experiments, end plates were fixed to the test section and placed 2 mm below the bottom of the cylinder (but not in contact with the cylinder), to encourage two-dimensional shedding, as discussed in Khalak & Williamson (1996).

A two-axis force balance utilizing LVDTs (linear variable displacement transducers) was used to measure lift and drag forces simultaneously with the measurement of displacement, while the displacement itself was measured using a non-contact (magnetostrictive) position transducer. In addition, the wake velocity field was also simultaneously measured, using DPIV. This is the first time, in free vibration, that force and wake vorticity have been simultaneously measured. All of the above measurements could be synchronized using a timing circuit that was triggered by the zero crossing of the position signal.

For the purpose of employing DPIV, the flow was seeded with 14-micron silver-coated glass spheres, which were illuminated by a sheet of laser light from a 5 W continuous argon ion laser. Images of the particles were captured using a high-resolution CCD Kodak Megaplus (1008 × 1018 pixels) camera, and transferred in real time to a PC. A mechanical shutter, in the path of the laser light, was used to reduce the exposure time of the frame, and to control the position of this exposure on the frame. This enabled acquisition of particle images that were separated by time periods less than the standard 33 ms, which corresponds with a camera operating at 30 Hz. This mechanical shutter was also controlled by the timing circuit mentioned earlier. Pairs of particle images were analysed using cross-correlation of sub-images described by Adrian (1991), and implemented digitally in the manner described by Willert & Gharib (1991) and Westerweel (1993). We used a two-step windowing process (with window shifting) to obtain particle displacements between image pairs, to deduce the velocity field. The viewing area of the camera was 28.4 cm × 28.7 cm (for the bigger diameter cylinder) and 12.8 cm × 12.93 cm (for the smaller cylinder), with corresponding time between images being 33 ms and 12.7 ms, respectively. In both cases, 64 × 64 pixel interrogation boxes were used for the first correlation followed by 32 × 32 pixel boxes for the second correlation. The number of particles in a 32 × 32 pixel window was approximately of the order of 15, high enough to give strong correlations, although the volume fraction of the tracer particles was very small, of the order of 2×10^{-6}. A box overlap of 50% was used in the second correlation, which resulted in a set of 3600 vectors (60 × 60) for a typical velocity field.

All the obtained images, and hence the DPIV velocity fields, were phase referenced

with respect to the position signal. This allowed possible phase averaging (over 10 cycles) of the velocity fields, along the lines of Gu *et al.* (1994). This is useful at the high Reynolds numbers of interest ($Re \sim 1000$ to 10 000) in the present study, to obtain a clear picture of the dynamics of spanwise vorticity, without the presence of smaller weak structures resulting from intermittent small-scale three-dimensionality in the flow.

Instantaneous amplitude, frequency and phase information shown in the paper have been computed with the use of the Hilbert transform (see Khalak & Williamson 1997 and Appendix in 1999 for details). In the case where there is intermittent switching between two modes, the instantaneous information from the Hilbert transform has been used to obtain separate values of the amplitude (as well as frequency and phase) corresponding to each of the modes, rather than averaging between the two modes.

The order of magnitude of the errors associated with some of the principal numerical quantities obtained from the present study are given in the text close to the relevant equations. Representative error bars are also indicated for selected data points that are used to compute such numerical quantities. In most other plots, the scatter between adjacent points gives an indication of the errors.

The origin of the coordinate system is fixed at the lowest position of the cylinder, at zero flow speed. The x-axis is downstream, the y-axis is perpendicular to the flow direction and to the cylinder axis (defined as transverse), and the z-axis lies along the axis of the cylinder (defined as spanwise).

3. Response and force measurements: case of low ($m^*\zeta$)

As described in the Introduction, the case of low ($m^*\zeta$) yields three principal branches of response, namely the initial, upper and lower branches. Our choice of parameters in this section, namely mass ratio, $m^* = 8.63$ and damping ratio, $\zeta = 0.00151$, leads to the peak amplitudes A^*_{max} for the upper and lower branches which are marked as bull's eye symbols in the Griffin plot of figure 2. The three principal response amplitude branches are denoted I (initial), U (upper) and L (lower) in figure 3. It might be noted that the initial branch is itself divided into a quasi-periodic sub-regime and a periodic sub-regime (as described further in Khalak & Williamson 1999). As normalized velocity U^* is increased, the amplitude jumps up from the initial to upper branch, reaching a maximum amplitude of $A^*_{max} \approx 0.85$, and thereafter the amplitude drops discontinuously from the upper to the lower branch ($A^*_{max} \approx 0.6$). As shown in Khalak & Williamson (1999), the initial $\leftrightarrow$ upper transition is hysteretic while the upper $\leftrightarrow$ lower transition involves an intermittent switching of modes. Outside these transition regions, each of the three response branches is close to being periodic as shown by typical time traces in figure 4 of cylinder displacement and phase (the phase being between total transverse force and displacement). Ultimately, at high $U^* \approx 10$, the wake becomes desynchronized, and the amplitude drops down to small values. It should be noted that in the intermittent upper $\leftrightarrow$ lower transition, in figure 3(*a*), care has been taken to separate upper and lower branch data, by the use of the Hilbert transform.

The corresponding frequencies of oscillation (f) for the different response branches are shown in figure 3(*b*). We may observe that over most of the synchronization regime ($U^* \sim 5.5$ up to 10), the frequency lies above unity ($f^* \approx 1.10$). This departure from unity might be expected if we recall equation (1.5):

$$f^* = \sqrt{\frac{(m^* + C_A)}{(m^* + C_{EA})}},$$

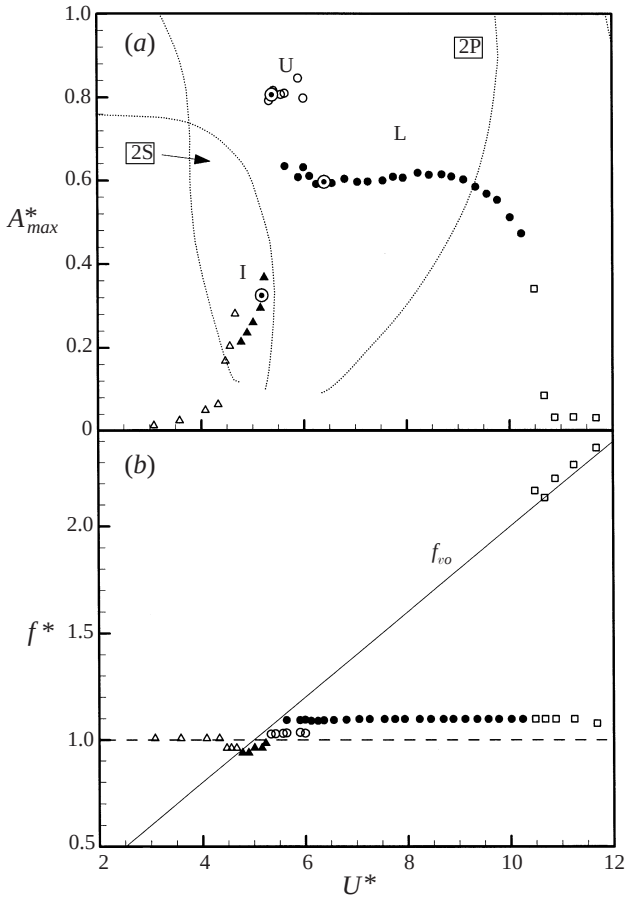

FIGURE 3. Amplitude (A^*) and frequency (f^*) response as a function of normalized velocity (U^*). At this low ($m^*\zeta$), three response branches are seen, namely the initial (I), upper (U), lower (L). Case of low ($m^*\zeta$) ($m^* = 8.63$, $\zeta = 0.00151$). △, Initial (quasi-periodic); ▲, initial (periodic); ○, upper; ●, lower; □, desynchronized regime; ⊙, location where the wake vorticity field is measured; ····· Williamson & Roshko (1988) map of wake modes. f_{vo} is the vortex shedding frequency in the absence of body oscillations.

and note that for low mass ratio, m^* becomes comparable to C_A and to C_{EA}, while C_{EA} is itself influenced by the force component in phase with body acceleration ($C_Y \cos\phi$).

3.1. *Classical use of total force* (C_Y) *and phase* (ϕ)

The transverse force commonly used in the literature is the total fluid force C_Y. The corresponding phase ϕ between total force and the displacement, as well as C_Y, are presented in figure 5(*a*), as a function of normalized velocity. The maximum transverse force (C_Y) occurs at the initial ↔ upper transition, after which it drops sharply at the upper ↔ lower transition. The corresponding phase angle ϕ remains slightly above 0° throughout the initial and upper branch regimes, and then jumps by almost 180° at the upper ↔ lower transition. Such a phase jump is well known in free vibrations, and has been previously inferred by Feng (1968) (one should note that he measures phase between a fluctuating surface pressure signal and the displacement), and it has been directly measured by Khalak & Williamson (1999). We shall see that this jump in ϕ

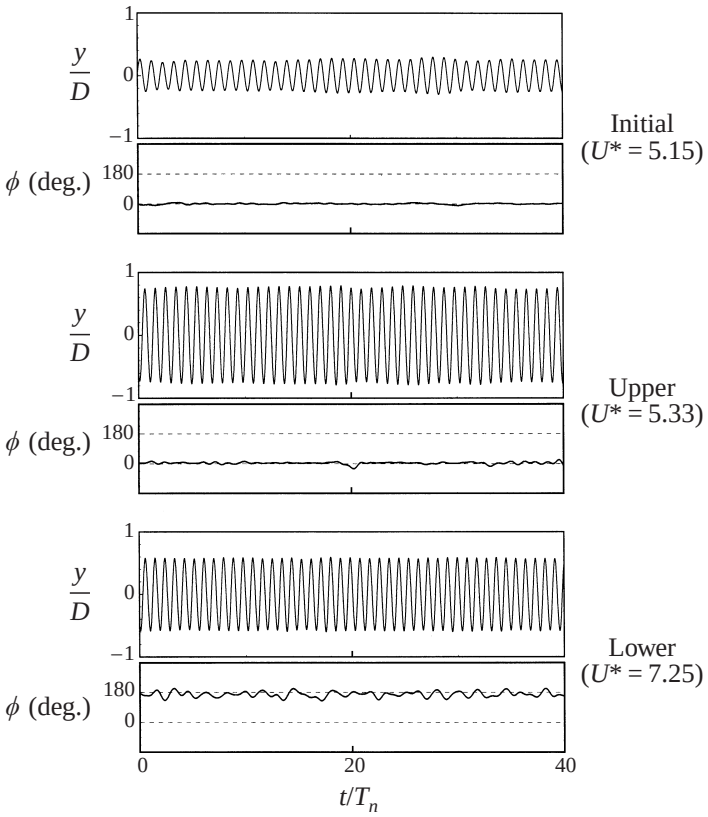

FIGURE 4. Typical time traces of cylinder displacement and phase ϕ (between total transverse force and displacement) in the initial, upper and lower branches. Case of low ($m^*\zeta$) ($m^* = 8.63$, $\zeta = 0.00151$).

is associated with the oscillation frequency (f) passing through the natural frequency of the structure in vacuum ($f_{N\,vacuum}$).

The equation of motion used to represent the body dynamics in equation (1.1) can be combined with equation (1.2), which assumes harmonic motion:

$$m\ddot{y} + c\dot{y} + ky = F_o \sin(\omega t + \phi). \tag{3.1}$$

Substituting $y = A\sin(\omega t)$ into the above equation and balancing $\sin(\omega t)$ terms, gives

$$\frac{F_o \cos\phi}{k\,A} = 1 - \left(\frac{f}{f_{N\,vacuum}}\right)^2, \tag{3.2}$$

where $f_{N\,vacuum} = 1/2\pi\sqrt{k/m}$. One may note from this simple result that, as ϕ jumps through the value of 90°, as one may observe in figure 5(*a*), then $f^*_{vacuum} = (f/f_{N\,vacuum})$ passes through 1.0. The above 'classical' phase jump has also been associated with a change in the timing of vortex shedding (Zdravkovich 1982). However, a *jump in this phase ϕ does not necessarily have to be associated with a switch in the timing of vortex shedding*. We shall prove this point in subsection § 3.2.

One may ask: how can one write the equation of motion in such a manner as to indicate *necessarily* when a jump in the timing of vortex formation may be found? A way to achieve this is to rewrite the equation of motion, retaining only the 'vortex

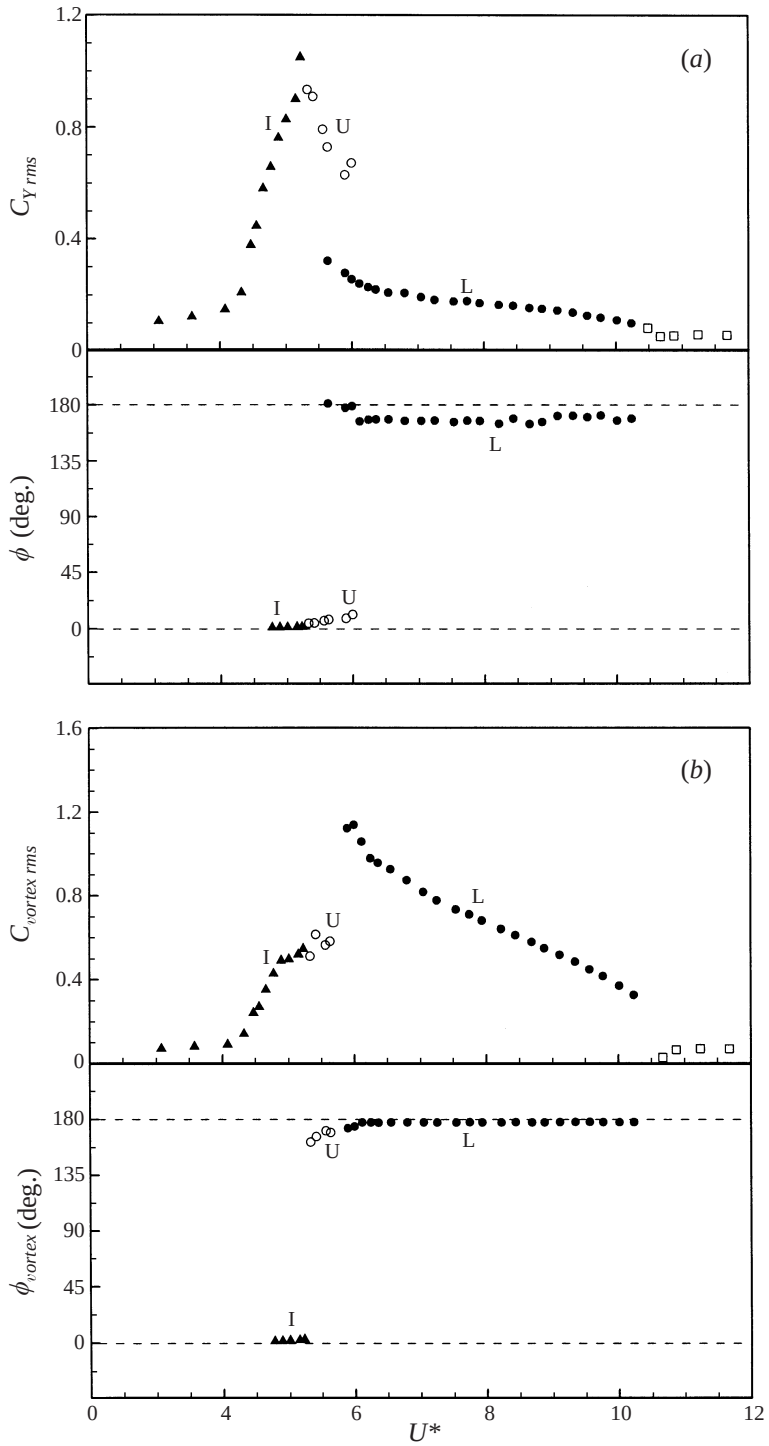

FIGURE 5. Force and phase angle variation with U^*: (*a*) total force and (*b*) vortex force. A large jump in ϕ occurs at the upper $\leftrightarrow$ lower transition, while there is a large jump in ϕ_{vortex} at the initial $\leftrightarrow$ upper transition. Case of low ($m^*\zeta$) ($m^* = 8.63$, $\zeta = 0.00151$). ▲, Initial (I); ○, upper (U); ●, lower (L); □, desynchronized regime.

force' on the right-hand side. ('Vortex force' is related to vortex formation and the convection of shed vorticity; Lighthill 1986). If the phase of this vortex force exhibits a jump, then necessarily we expect a jump in the timing of vortex shedding. We shall use this approach in the next section.

3.2. *Vortex force* (C_{vortex}) *and vortex phase* (ϕ_{vortex})

It was shown by Lighthill (1986) that the total fluid force (F_{total}) can be conveniently decomposed into a 'potential force' component $F_{potential}$, given in this case by the potential added-mass force, and a 'vortex force' component (F_{vortex}) that is due to the dynamics of what is called the 'additional vorticity.' ('Additional vorticity' refers to the entire vorticity in the flow field minus 'part of the distribution of vorticity attached to the boundary in the form of a vortex sheet allowing exactly the tangential velocity (slip) associated with the potential flow,' as stated by Lighthill. A full knowledge of the vorticity field would yield the vortex force through the concept of vorticity impulse: $\boldsymbol{F}_{vortex} = -\frac{1}{2}\rho(\mathrm{d}/\mathrm{d}t)\int(\boldsymbol{x}\times\boldsymbol{\omega}_a)\,\mathrm{d}V$, where $\boldsymbol{\omega}_a$ is the additional vorticity. This decomposition of the flow field to yield a potential force and vortex force can be understood to be a matter of convenience, although it is very useful in the present context. The vortex force is related in a definite way to vortex dynamics, and to the convection of vorticity. Any jumps in vortex force would necessarily correspond with sharp changes in the process of vortex formation.

For convenience, we now drop the subscript ($_Y$) to denote the transverse force. The vortex force F_{vortex}, can thus be computed from

$$F_{vortex} = F_{total} - F_{potential}. \tag{3.3}$$

Normalizing all the forces by ($\frac{1}{2}\rho U^2 DL$) gives the simple equation

$$C_{vortex}(t) = C_{total}(t) - C_{potential}(t). \tag{3.4}$$

The instantaneous potential added-mass force $F_{potential}$ acting on the cylinder is given by

$$F_{potential}(t) = -[C_A\, m_d\, \ddot{y}(t)], \tag{3.5}$$

where m_d is the displaced fluid mass: $m_d = (\pi\rho D^2 L/4)$. Normalizing this force by ($\frac{1}{2}\rho U^2 DL$), and substituting for $y = A\sin(t)$, we find the potential force coefficient is given by

$$C_{potential}(t) = 2\pi^3 \frac{\big(y(t)/D\big)}{\big(U^*/f^*\big)^2}. \tag{3.6}$$

It can be seen from the above equation that the instantaneous potential added-mass force $C_{potential}(t)$ is always *in-phase* with the cylinder motion $y(t)$, as one might expect.

Let us now introduce an equation of motion where the fluid force retained on the right-hand side is the vortex force only. (Henceforth, any force $F(t)$ refers to the instantaneous force, otherwise F refers to the magnitude of this force).

Equation of motion using 'vortex force':

$$(m + m_A)\ddot{y} + c\dot{y} + ky = F_{vortex}\sin(\omega t + \phi_{vortex}). \tag{3.7}$$

(As an aside, the absorption of the added mass (m_A) into the total oscillating mass has sometimes been used in texts on fluid–structure interactions (e.g. Blevins 1990; Sumer & Fredsøe 1997), and sometimes it is left on the right-hand side of the equation of motion, as in Bearman's (1984) review. However, in many cases, the fluid force

is uniformly described as the 'lift force', whether it includes or excludes the 'added mass.' There is often no apparent reason to choose one approach or the other, and these differences have been the subject of debate. In this work, we purposefully adopt both approaches simultaneously.) The point here is to highlight the 'vortex phase', ϕ_{vortex}, defined as the phase between vortex force and displacement. For the sake of clarity, we rewrite here the original equation of motion, but now defining total force as F_{total}, and writing the 'classical' phase ϕ, as the 'total phase' ϕ_{total}:

Equation of motion using 'total force':

$$m\ddot{y} + c\dot{y} + ky = F_{total} \sin(\omega t + \phi_{total}). \tag{3.8}$$

We have thus defined two distinct phases, which are reiterated below for clarity:

'VORTEX PHASE' $= \phi_{vortex}$ = Phase between VORTEX force and displacement,
'TOTAL PHASE' $= \phi_{total}$ = Phase between TOTAL force and displacement.

Interestingly, there is no clear jump in 'vortex phase' ϕ_{vortex} at the upper–lower branch transition, as may be seen in figure 5(*b*), contrary to one's expectation, based on past studies, such as Zdravkovich (1982). Therefore one might suspect that the modes of vortex formation between upper and lower branches are similar. This 'clue' will be confirmed later from our vorticity flow field measurements. On the other hand, between the initial and upper branches, there *is* a vortex phase jump. There will necessarily be a switch in timing of the cyclic vortex formation, which is also later confirmed by flow field measurements. There are thus *two* phase jumps: namely a large jump in vortex phase (ϕ_{vortex}) at the initial $\leftrightarrow$ upper transition, which is associated with a switch in the timing of vortex shedding; and a large jump in total phase (ϕ_{total}), at the upper $\leftrightarrow$ lower transition, which is *not* associated with a switch in timing of the shedding.

A striking feature of the variation in vortex force (C_{vortex}), in figure 5(*b*), is the peak in the lower branch, despite the total force (C_{total}) having rather small values. Although this seems surprising at first, it is actually reasonable to expect a small total force C_{total}, as there is a considerable amount of cancellation between the out-of-phase $C_{vortex}(t)$ and the in-phase $C_{potential}(t)$, as shown in the lower-branch force signals of figure 6.

Typical relationships between potential force, vortex force and the total force, for the three different response branches, are shown in figure 6. (These time traces are the result of averaging over 10 cycles). Each case in figure 6 corresponds with the data points marked by a 'bull's eye' in the amplitude response plot of figure 4(*a*) at three different U^*. One can now understand the total force magnitude for the different response branches, as observed in figure 5. In the initial branch, the total force reaches a large value, because the vortex force component C_{vortex} and the potential force component $C_{potential}$ are in phase. In the upper branch, although C_{vortex} and $C_{potential}$ are out of phase, the large amplitude of this branch causes a large potential force, which far exceeds the vortex force, leading to a large total force. Finally, in the lower branch, the out-of-phase force components become quite comparable, and the total force is quite diminished.

It was shown earlier that the jump in total phase ϕ_{total} was associated with $f^*_{vacuum} = (f/f_{N\,vacuum}) = 1.0$. One might question what frequency condition holds when ϕ_{vortex} jumps. Inspecting the equation of motion using 'vortex force' in (3.7),

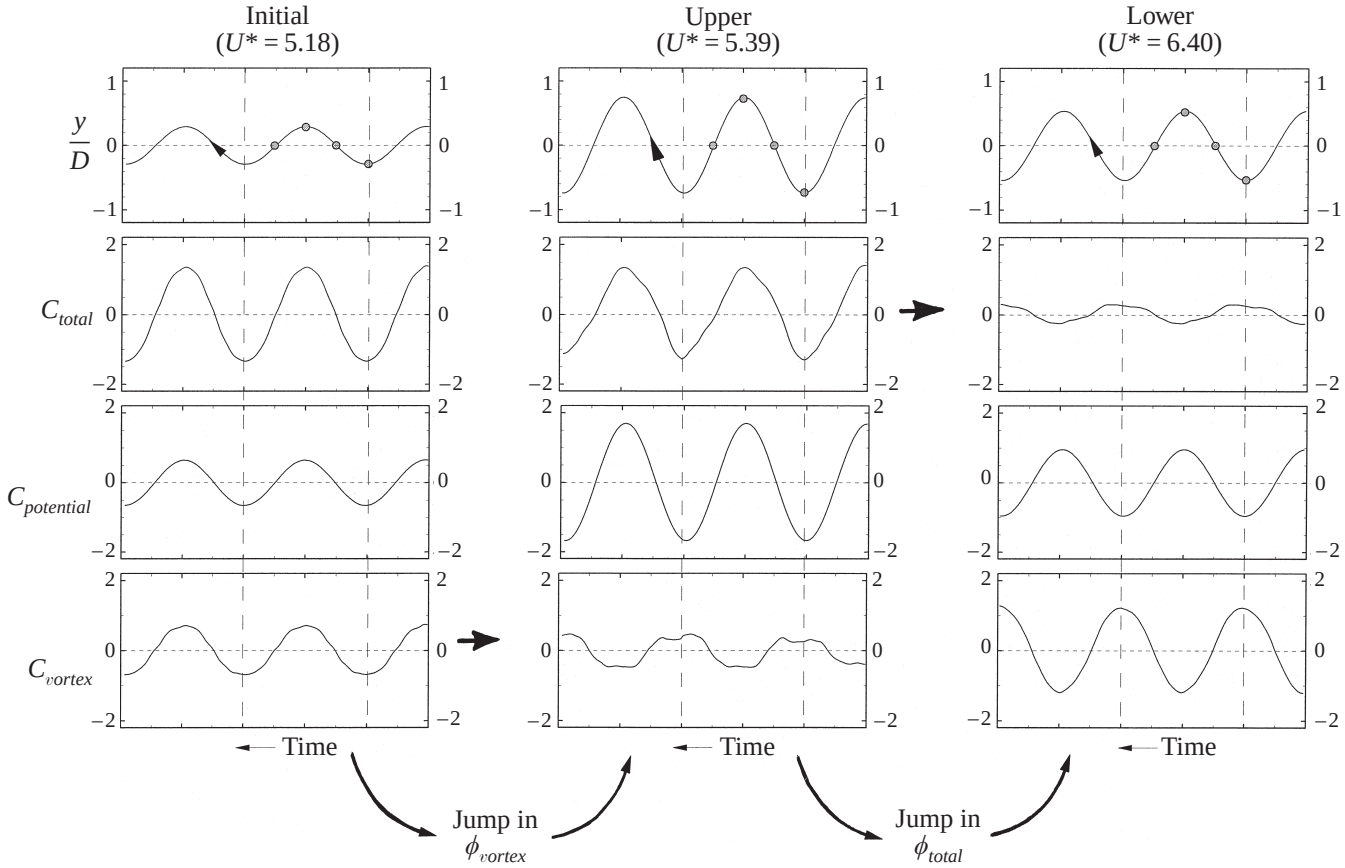

FIGURE 6. Relationship between total transverse force (C_{total}), the potential added mass force ($C_{potential}$), and the vortex force (C_{vortex}) in the three response branches. Low ($m^*\zeta$) ($m^* = 8.63$, $\zeta = 0.00151$).

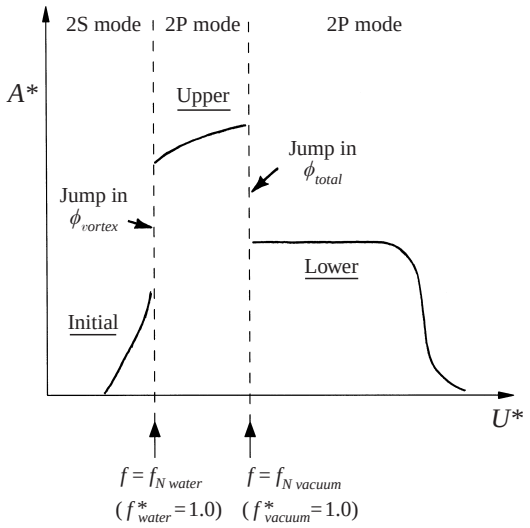

FIGURE 7. Schematic diagram of the low-($m^*\zeta$) type of response showing the three principal branches (initial, upper and lower), and correspondingly the two jump phenomena.

and using similar textbook results as for equation (3.2) earlier, we find

$$\frac{F_{vortex}\cos\phi_{vortex}}{k\,A} = 1 - \left(\frac{f}{f_{N\,water}}\right)^2. \tag{3.9}$$

Therefore, as ϕ_{vortex} jumps through 90°, as observed in figure 5(b), then $f^*_{water} = (f/f_{N\,water})$ passes through 1.0. This condition on f^*_{water} (or f^*) is evident from figure 3(b) at the initial ↔ upper transition.

A summary sketch is included in figure 7, to show with clarity how there are two distinctly different jumps between modes, in contrast with the classical high-($m^*\zeta$) type of vibration where only a single mode jump is observed. In essence, the mode change initial → upper is associated with a jump in vortex phase ϕ_{vortex}, as the response frequency passes through $f^*_{water} = f/f_{N\,water} = 1.0$. The second mode change upper → lower corresponds with a jump in total phase ϕ_{total}, as the response frequency passes through $f^*_{vacuum} = f/f_{N\,vacuum} = 1.0$.

To make very clear this significant point regarding mode transitions we include a shorthand summary:

Initial ↔ upper transition:

$$\left[\frac{f}{f_{N\,water}}\right] \sim 1 \quad \Rightarrow \quad f^*_{water} \sim 1 \Rightarrow \phi_{vortex}\ \text{JUMP}.$$

Upper ↔ lower transition:

$$\left[\frac{f}{f_{N\,vacuum}}\right] \sim 1 \quad \Rightarrow \quad f^*_{vacuum} \sim 1 \Rightarrow \phi_{total}\ \text{JUMP}.$$

As a final point, we show here how one of the phases (say, ϕ_{vortex}) may experience a large jump, while the other phase (ϕ_{total}) might not exhibit any significant change. Let us consider the two equations of motion (3.7) and (3.8), and write equations for the relevant phases (as may be found in many dynamics texts; see for example Naudascher & Rockwell 1994, p. 10) as follows.

The equation of motion using 'vortex force'

$$(m + m_A)\ddot{y} + c\dot{y} + ky = F_{vortex} \sin(\omega t + \phi_{vortex})$$

gives an equation for ϕ_{vortex} as

$$\tan \phi_{vortex} = \left[\frac{2\zeta f^*_{water}}{1 - {f^*_{water}}^2} \right]. \tag{3.10}$$

The equation of motion using 'total force'

$$m\ddot{y} + c\dot{y} + ky = F_{total} \sin(\omega t + \phi_{total})$$

gives an equation for ϕ_{total} as

$$\tan \phi_{total} = \left[\frac{2\zeta f^*_{vacuum}}{1 - {f^*_{vacuum}}^2} \right]. \tag{3.11}$$

We shall first consider the low-$(m^*\zeta)$ type of response, where there are two distinct mode transitions. Taking the first mode transition, equations (3.10) and (3.11) show that as f^*_{water} jumps through 1.0, the phases change typically as follows (noting here that ζ is very small):

$$\begin{aligned} (\tan \phi_{vortex}) \text{ jumps from [small } +] &\rightarrow [\text{small} -], \\ (\tan \phi_{total}) \text{ jumps from [small } +] &\rightarrow [\text{slightly bigger } +]; \end{aligned}$$

$$\begin{aligned} \phi_{vortex} \text{ jumps from } [5^\circ] &\rightarrow [175^\circ] \Rightarrow \text{LARGE JUMP in } \phi_{vortex}, \\ \phi_{total} \text{ jumps from } [5^\circ] &\rightarrow [6^\circ] \Rightarrow \text{small change in } \phi_{total}. \end{aligned}$$

(Angles in degrees are for illustration only, and are not precise.)

Looking now at the second mode transition, as f^*_{vacuum} passes through 1.0, typical changes in phase are

$$\begin{aligned} (\tan \phi_{vortex}) \text{ jumps from [small } -] &\rightarrow [\text{small} -], \\ (\tan \phi_{total}) \text{ jumps from [small } +] &\rightarrow [\text{small} -]; \end{aligned}$$

$$\begin{aligned} \phi_{vortex} \text{ jumps from } [175^\circ] &\rightarrow [176^\circ] \Rightarrow \text{small change in } \phi_{vortex}, \\ \phi_{total} \text{ jumps from } [5^\circ] &\rightarrow [175^\circ] \Rightarrow \text{LARGE JUMP in } \phi_{total}. \end{aligned}$$

We conclude that, at the first mode transition, ϕ_{vortex} experiences a massive jump of around π. On the other hand, the total phase ϕ_{total} indeed jumps, but by an almost imperceptibly small amount. At the second mode transition, ϕ_{total} jumps significantly by around π, while in this case ϕ_{vortex} jumps almost imperceptibly. Thus, the *large* jumps are only for ϕ_{vortex} at the first mode transition, and for ϕ_{total} at the second mode transition.

Finally, in the case of high $(m^*\zeta)$, for example for the Feng-type experiments in figure 8, it is apparent that both phases, ϕ_{vortex} and ϕ_{total}, exhibit a large jump at the mode transition initial $\leftrightarrow$ lower. If we now look ahead to the frequency response for high $(m^*\zeta)$ in figure 8(*c*), we see the interesting result that the *oscillation frequency jumps through both* $f_{N\,water}$ *and* $f_{N\,vacuum}$ *at the same point*, inducing simultaneous jumps in both ϕ_{vortex} and ϕ_{total}. This further identifies the two-mode high-$(m^*\zeta)$ type of response as being quite distinct from the three-mode low-$(m^*\zeta)$ type of response. We shall briefly study the high-mass–damping type of response in the next section.

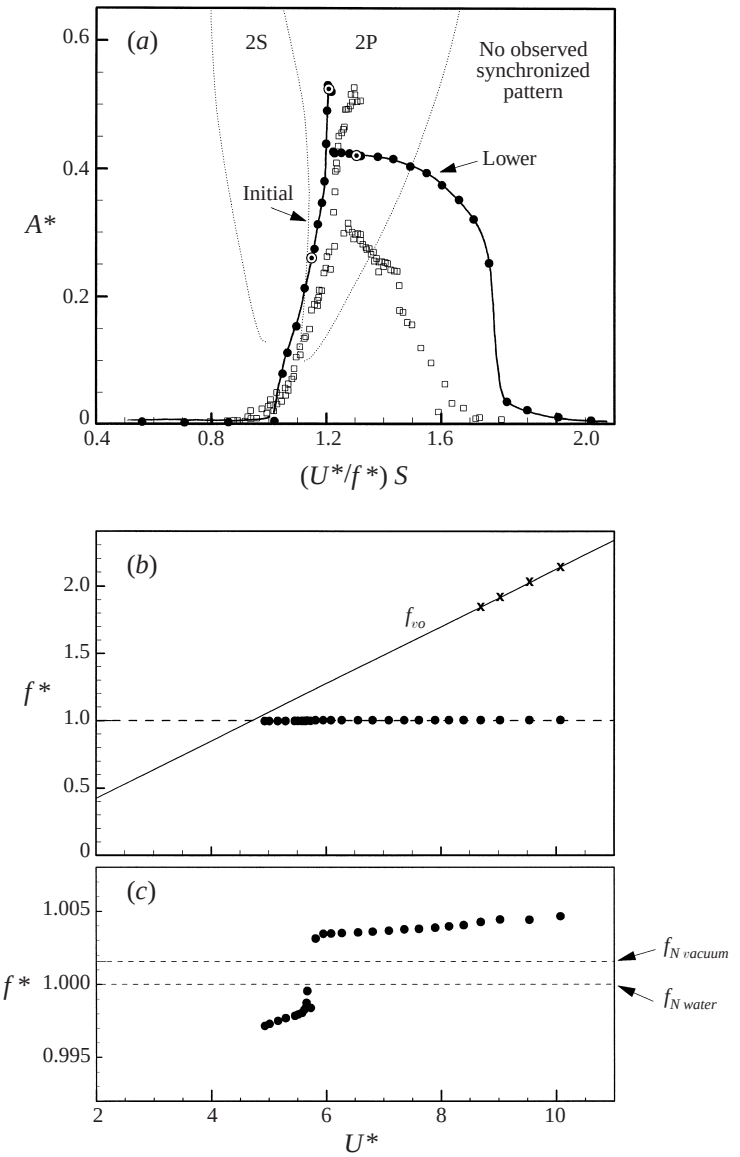

FIGURE 8. Amplitude (A^*) and frequency (f^*) response as a function of normalized velocity (U^*). At this high ($m^*\zeta$), two response branches are seen, namely the initial and lower branches. Case of high ($m^*\zeta$) ($m^* = 320$, $(m^* + C_A)\zeta = 0.251$). An enlarged view of the frequency data in (c) indicates a small but distinct jump in f^* at the initial $\leftrightarrow$ lower transition. ●, Present data; □, Feng (1968); · · · ·, Williamson & Roshko (1988) map of wake modes; ⊙, points where wake vorticity is measured. In (b) ×, transverse force frequency in the desynchronized regime.

4. Response and force measurements: case of high ($m^*\zeta$)

In contrast to the low-($m^*\zeta$) type of response, the high-($m^*\zeta$) one exhibits only two distinct branches of response, namely the initial and lower branches, the upper branch being absent here. The mass–damping parameter for this case, $(m^* + C_A)\zeta = 0.251$, has been specifically chosen to be very close to the mass–damping of Feng (1968) for his lowest-damped case, as shown in the Griffin plot of figure 2. It should also be

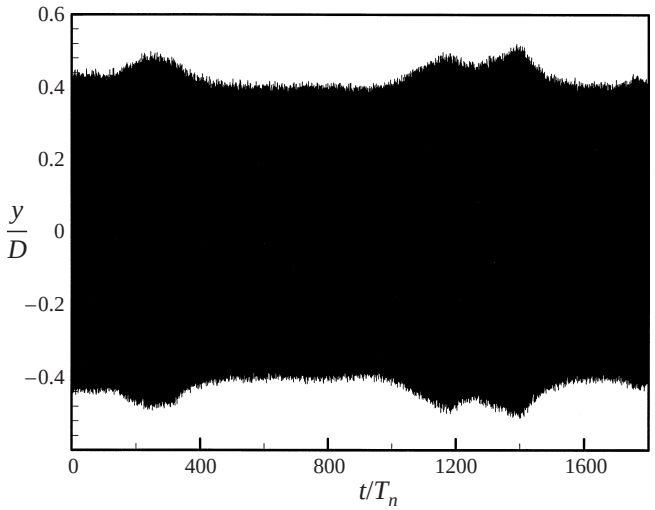

FIGURE 9. Initial ↔ lower branch transition. High-($m^*\zeta$) case. Time trace of displacement showing an intermittent switching between the two modes, occurring over enormous time scales ($U^* = 5.73$).

noted that the higher value of amplitude A^*_{max} in the Griffin plot corresponds with the peak amplitude of the initial branch (the left-hand response branch in figure 8*a*), while the smaller A^*_{max} in the Griffin plot is the peak amplitude of the lower-branch response (the right-hand branch in figure 8*a*). As normalized velocity is increased, the initial-branch amplitude rises continuously to the maximum response amplitude $A^*_{max} \approx 0.52$, and thereafter the amplitude drops sharply to $A^*_{max} \approx 0.42$ in the lower branch. This transition from initial → lower branch involves an intermittent switching between the two modes, with a very long time period of switching, of the order of a few hundred oscillation cycles, as shown in the time trace of figure 9. (This would make it somewhat problematic to detect in DNS computations.)

Comparing our amplitudes to those of Feng (1968), also shown in figure 8(*a*), we find a very similar behaviour in the initial branch, with almost exactly the same value, $A^*_{max} \approx 0.52$, for the peak amplitude reached. However, in the lower branch our amplitudes are substantially larger than those of Feng. The reason for this difference is not known, but it might be associated with the fact that no end plates were used in Feng's experiment to maximize spanwise correlation. This difference in amplitudes could in turn be the cause of the difference in the type of transition between the initial and lower branches, from hysteretic in Feng's case to intermittent switching in our case.

The amplitude response of figure 8 is overlaid by the boundaries for different vortex formation modes, as found from forced-vibration studies in Williamson & Roshko (1988). Corresponding to their suggestions, this indicates that the continuous initial branch will be associated with the 2S mode, and the lower branch will be associated with the 2P mode, although the boundaries may need to be shifted slightly to take into account the different Reynolds numbers. We shall show later from DPIV vorticity measurements that the initial branch indeed corresponds with the 2S mode of vortex wake, while the lower branch corresponds with the 2P mode.

The corresponding frequency response f^*, shown in figure 8(*b*), is quite different from the low-($m^*\zeta$) case, and remains close to unity over the entire range of synchronization. This scenario is to be expected, because the large mass ratio

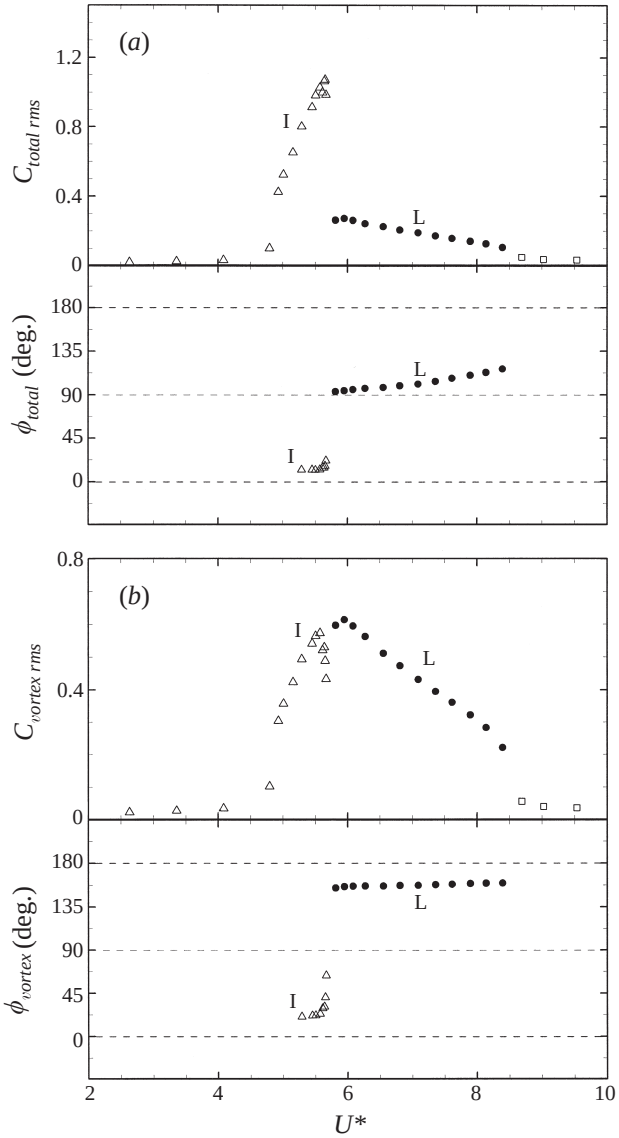

FIGURE 10. Force and phase angle variation with U^*: (*a*) total force and (*b*) vortex force. A simultaneous large jump in ϕ_{total} and ϕ_{vortex} occurs at the initial ↔ lower transition. Case of high $(m^*\zeta)$ $(m^* = 320, (m^* + C_A)\zeta = 0.251)$. △, Initial branch (I); ●, lower branch (L); □, desynchronized regime.

$m^* = 320 \gg C_A, C_{EA}$; and from equation (1.5), $f^* \approx 1.0$. Interestingly, even after the wake is desynchronized, the cylinder oscillation frequency (f) does not jump back to the non-oscillating vortex shedding frequency (f_{vo}), but remains close to f_N (i.e. $f^* = f/f_N \approx 1$). On the other hand, the peak frequency in the transverse force spectrum follows closely the non-oscillating shedding frequency (f_{vo}) when the wake de-synchronizes. Feng (1968) found a similar behaviour in his frequency variation in the de-synchronized regime, the only difference being that in his case, the peak frequency was obtained from the spectrum of a fluctuating surface pressure signal, rather than from direct force measurements.

Simultaneous jumps in phases ϕ_{vortex} and ϕ_{total}, for this high-($m^*\zeta$) case, are shown in the force and phase plots of figure 10, which correspond with f^* jumping across both $f_{N\,water}$ and $f_{N\,vacuum}$ at the same point in figure 8(*c*) (see discussion in § 3). The forces C_{total} and C_{vortex}, in general show behaviour qualitatively similar to that seen in corresponding branches of the low-($m^*\zeta$) case, the maximum C_{total} being in the initial branch while the maximum C_{vortex} is reached in the lower branch.

In the low-($m^*\zeta$) case, considered earlier in § 3, we thus find two jumps since there are three branches of response. The first transition represents a large jump in ϕ_{vortex}, while the second transition involves a large jump in total phase ϕ_{total}. In the present, and more classical, case of high ($m^*\zeta$), there are only two response branches and only one mode transition, comprising simultaneous large jumps in both ϕ_{vortex} and ϕ_{total}. This case therefore corresponds with the classical scenario, whereby the jump between modes is simultaneously associated with a switch in the timing of vortex shedding. This point is proven from vorticity measurements in the next section.

5. Modes of vortex formation

There has been some debate concerning the vortex formation modes that might be associated with the different response branches, as outlined in the Introduction. For the high-($m^*\zeta$) case, there is some flow visualization from Brika & Laneville (1993) to suggest that the initial branch is associated with the 2S mode, while the lower branch comprises the 2P mode. Similar observations by Khalak & Williamson (1999) have been made for the case of low ($m^*\zeta$). Such hydrogen bubble and dye visualizations are quite unclear at these Reynolds numbers (10^3–10^4), and perhaps may only be construed as suggestive of the dominant wake pattern. Visualization was also not sufficiently clear to determine the wake formation mode for the upper branch, in Khalak & Williamson (1999), and was not included in that work. Therefore, in this section, we use DPIV to study the wake vorticity fields for each response branch. These are the first DPIV measurements (performed simultaneously with force measurements) that have been made for vortex-induced vibration of a cylinder. We shall find a good correspondence with a 'clue' which appeared in § 3, namely that there exists a 'vortex phase' jump for the initial ↔ upper transition, suggesting the initial and upper wake modes are different, whereas there is no such jump for the upper ↔ lower transition, suggesting that the vortex wake modes of the upper and lower branch are the same.

5.1. *Low mass–damping type of response*

Sequential vorticity fields during a cycle of oscillation for the initial branch clearly exhibit the classical 2S vortex formation mode as shown in figure 11. The dynamics of the concentrated regions of vorticity follow a pattern similar to what is found in a classical von Kármán street. It may be noted that the vorticity fields for each branch in figures 11–13 correspond with the 'bull's eye' data points in figure 3(*a*).

The upper-branch sequence in figure 12 exhibits quite a different wake mode, which is, in essence, a 2P mode. As the body is moving downward in (*a*), the lower (red) anticlockwise vorticity concentration, which forms due to the roll-up of the lower shear layer, is deformed and split into two parts. The upper part forms a weak anticlockwise vortex beside the much stronger blue clockwise vortex, thus forming a vortex pair. A similar process of deforming and splitting, for a blue vortex, is seen as the body moves upwards in (*b*) and (*c*), forming a second vortex pair in the cycle of motion. However, the second vortex of each vortex pair is rapidly weakened by the relatively stronger first vortex. This is probably due to the intense strain of

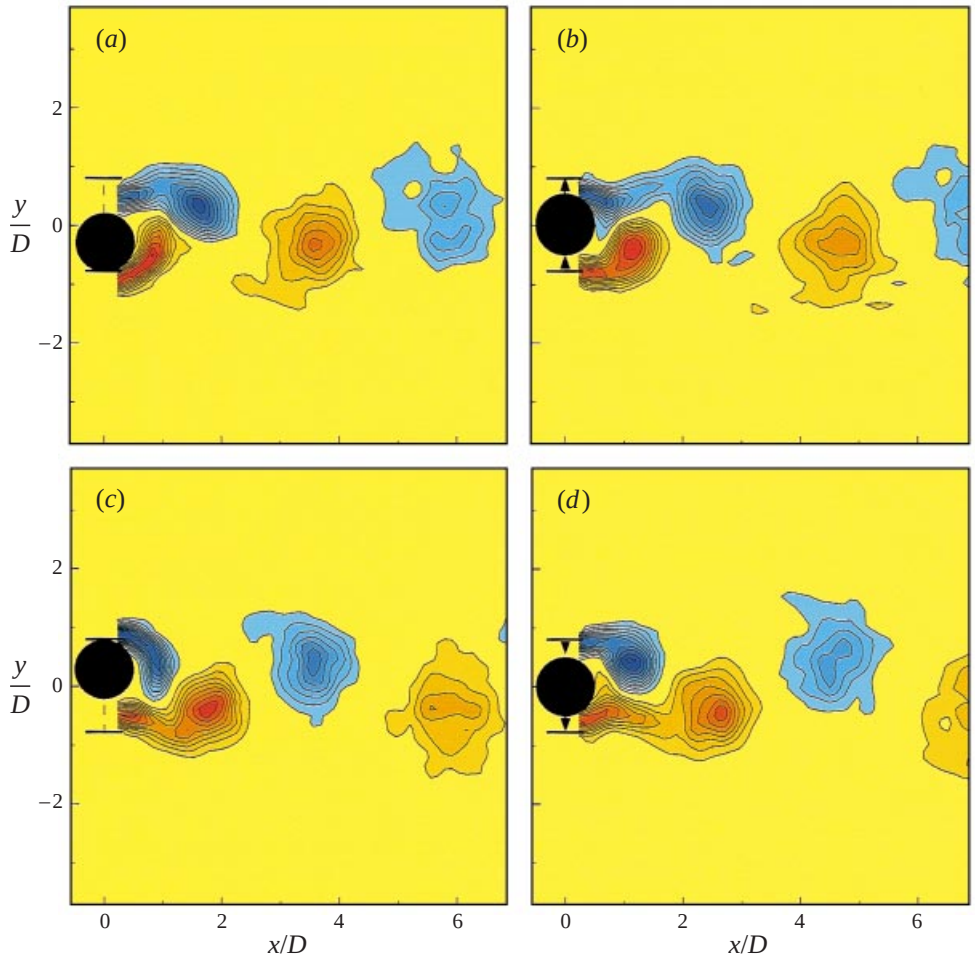

FIGURE 11. Initial-branch vorticity plots, showing the 2S mode, for low ($m^*\zeta$). Each of these plots from DPIV is separated by a quarter-period. Blue contours show clockwise vorticity, red anticlockwise vorticity. Contour levels shown are $\omega D/U = \pm 0.4, \pm 0.8, \pm 1.2, \ldots$. $U^* = 5.18$, $A^* = 0.33$ as for $\odot$ symbol of figure 3(*a*). $Re \approx 3000$.

the larger vortex on the weaker vortex. The fact that this wake mode, as it travels downstream, begins to take on the appearance of a 2S pattern now explains the difficulty experienced in using flow visualization to interpret this mode in Khalak & Williamson (1999). The observation of the 2P mode of wake formation is consistent now with the fact that the upper branch appears within the 2P mode region in the overlaid Williamson–Roshko (1988) map of wake modes in figure 3.

The fact that there is a jump in the 'vortex phase', ϕ_{vortex}, for the initial $\leftrightarrow$ upper transition is consistent with the 2S $\leftrightarrow$ 2P vortex mode jump. On the other hand, the absence of a large jump in ϕ_{vortex} across the upper $\leftrightarrow$ lower transition would suggest that the wake modes for these branches are similar. This is indeed the case, as may be seen by observing the 2P mode of wake formation for the lower branch in figure 13. Again one finds deformation, stretching and splitting of the main vorticity concentrations, for example as we see in the case of the red vorticity in (*a*), or the blue vorticity in (*c*), which lead to the formation of vortex pairs. However, the second

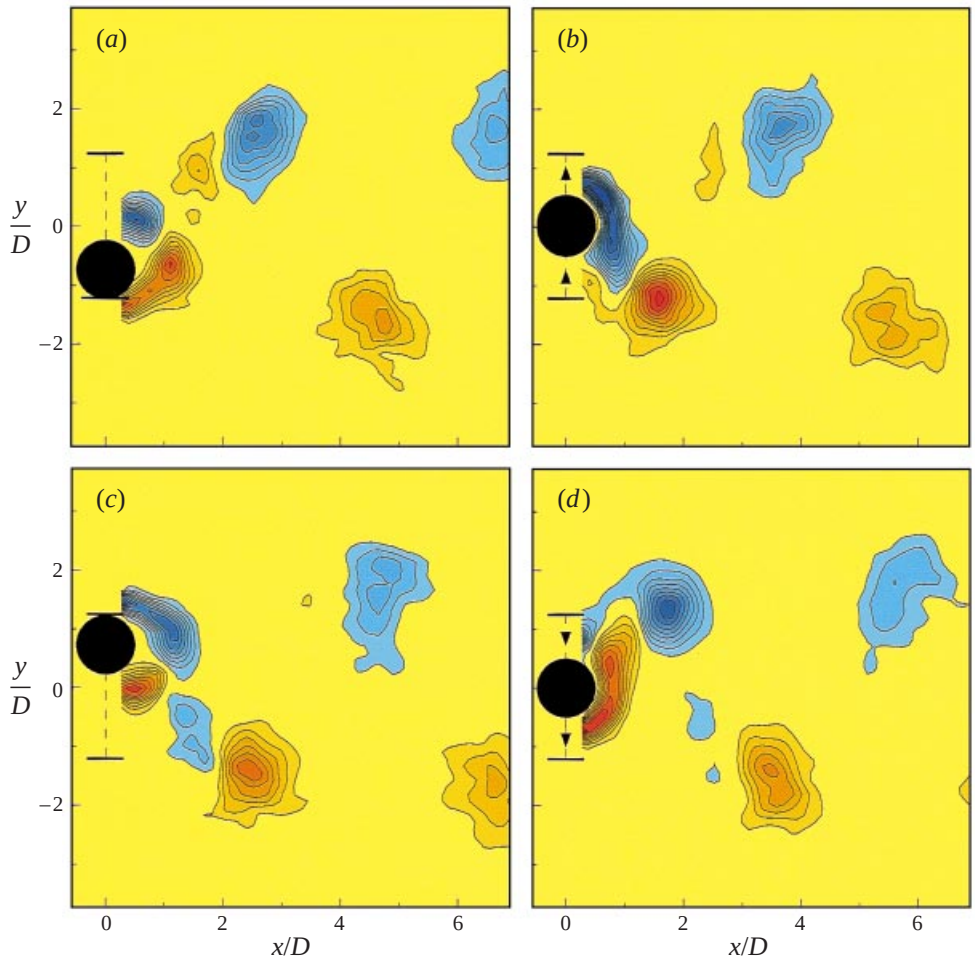

FIGURE 12. Upper-branch vorticity plots, showing the 2P mode, for low ($m^*\zeta$). In this 2P mode, there are two vortex pairs formed per cycle, although the second vortex of each pair is much weaker (20%) than the first vortex, and decays rapidly. (Contour levels are as for figure 11. $U^* = 5.39$, $A^* = 0.81$, $Re \approx 3100$.)

vortex of each pair is now considerably stronger than the equivalent second vortex in the upper-branch 2P mode in figure 12. It is clear that the 2P mode is associated with the splitting of a region of vorticity in each half-cycle, as discussed from forced vibrations in Williamson & Roshko (1988). In Appendix A, we use DPIV to compute the most intense strain rate regions for the different modes here, indicating how for the 2P mode these are located within the primary vorticity concentrations thereby inducing the characteristic vortex splitting.

As discussed in the Introduction, a number of accurate simulations at low Reynolds numbers ($Re \sim 100$–200), and two-dimensional simulations at higher $Re \sim 500$ (Blackburn & Henderson 1999), as well as some experiments, do not find this 2P mode. This mode is found as a transient, interchanging with the P + S mode, in the work of Evangelinos & Karniadakis (1999). This has led to some debate about the existence of this 2P mode as a *steady-state* pattern. In order to resolve this debate, we have included additional material (Appendix B) that provides proof to show that

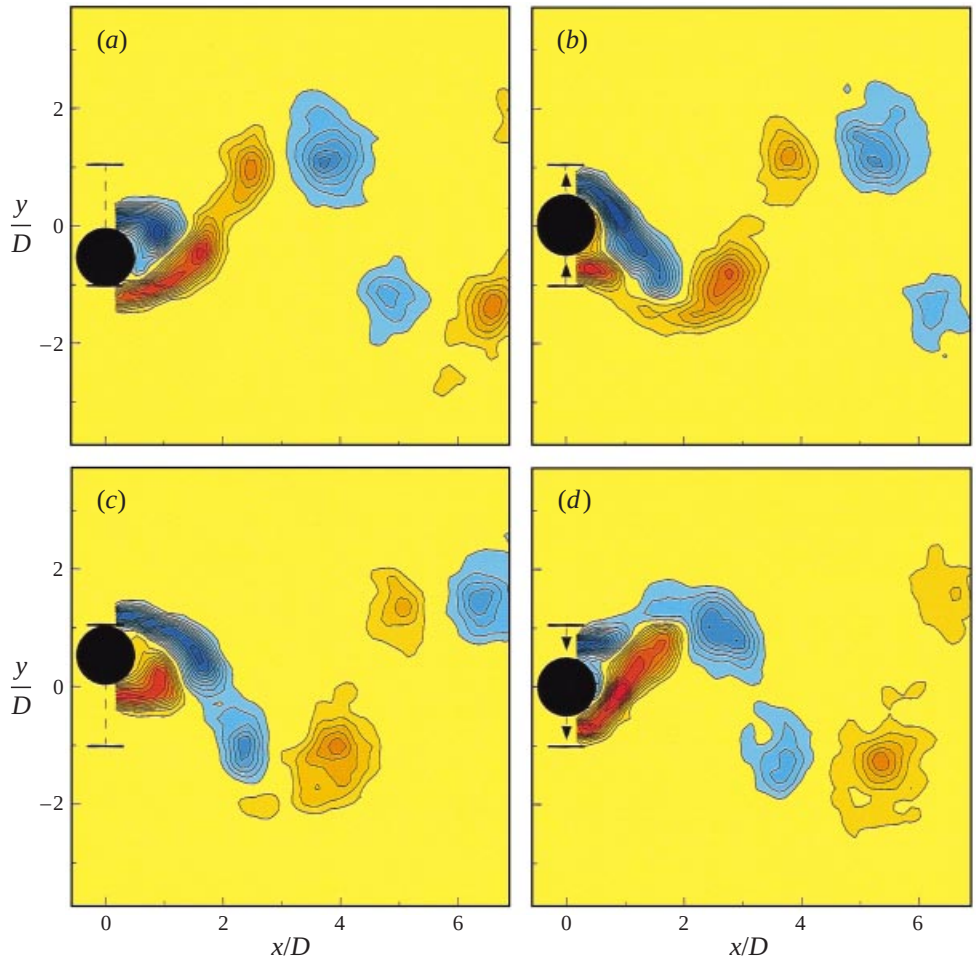

FIGURE 13. Lower-branch vorticity plots, showing the 2P mode, for low ($m^*\zeta$). In this 2P mode, the second vortex of each vortex pair is now quite comparable (60%) to the first vortex pair. (Contour levels are as for figure 11. $U^* = 6.40$, $A^* = 0.60$, $Re \approx 3700$.)

this 2P pattern continues indefinitely for the lower branch case presented here. The apparent disparity between high Reynolds number experiments ($Re \sim 2000$ to 4000) and the simulations seems to be a Reynolds number effect.

It is clear that there is a change in the pattern of vortex formation between the initial and upper branches, consistent with the jump in 'vortex phase', ϕ_{vortex}, between these branches. In order to illustrate the change in the timing of vortex shedding between these branches, we show in figure 14(*a*) the vorticity concentrations when the body is at the centre of its lateral oscillation. However, we choose to illustrate the body moving down for the initial branch, and the body moving up for the upper branch. Although the images are relatively half a cycle different, the near-wake vorticity concentrations are similar: in each case the lower red (anticlockwise) vortex has just been shed. In other words, there is a switch in the timing of vortex shedding by around 180° as the modes change 2S ↔ 2P at the initial ↔ upper transition, which corresponds well with the jump in phase of the 'vortex force', ϕ_{vortex}, by about 180° at this transition.

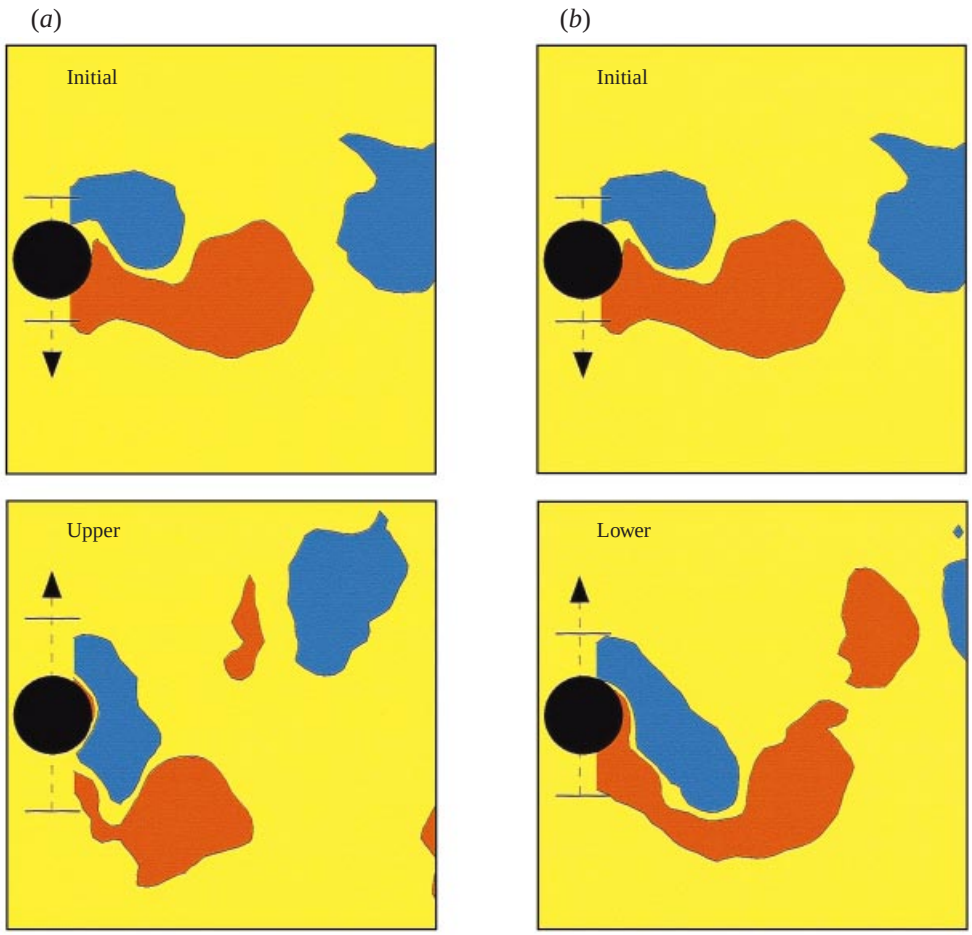

FIGURE 14. Switch in timing of vortex shedding between different vortex formation modes. There is a switch of around 180° in the timing of vortex shedding between the initial and upper branches in (*a*), and between the initial and lower branches in (*b*). This indicates also that the upper and lower branches are in phase with each other. Please note the direction of travel of the body in each of these images.

A comparison between the initial- and lower-branch vorticity fields in figure 14(*b*) again shows similar near-wake vorticity dynamics for body motions that are 180° apart. In other words, there is again roughly a 180° phase shift in the timing of vortex shedding. These comparisons in (*a*) and (*b*) indicate that the upper and lower branches have a similar timing of vortex formation, which corresponds well with the absence of any large jump in the 'vortex phase' ϕ_{vortex} between the branches, and with the fact that the wake formation modes are the same. The 'vortex phase' is therefore a valuable tool to indicate broadly the timing of vortex formation in these problems, and is being used extensively in ongoing studies.

We shall proceed to look at the circulation strengths of the shed vortices in these repeatable wake modes, as shown in figure 15. All the circulation strengths are calculated at the instant when an entire shear layer of one sign is just about to be shed (for example figure 13(*b*), for the red counter-clockwise vorticity). The dashed line marked as 'static', in figure 15, indicates the circulation strength of the

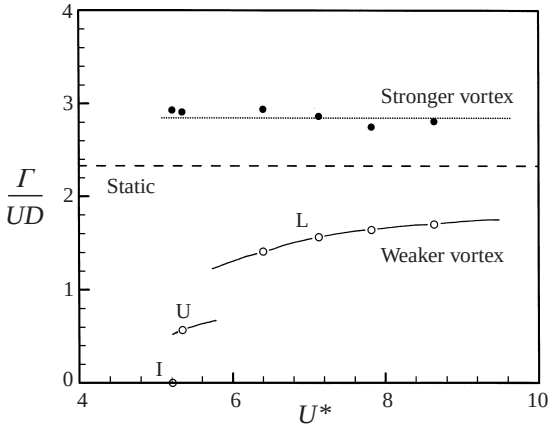

FIGURE 15. Variation of the circulation strength (Γ) of the shed vortices as a function of the normalized velocity U^*: ●, stronger vortex; ○, weaker vortex.

vortices $\Gamma^* = \Gamma/UD = 2.33$, corresponding to the stationary cylinder case measured at $Re = 3900$. This value is in reasonable agreement with those of Chyu & Rockwell (1996), and Lin, Vorobieff & Rockwell (1995) at $Re \sim 10\,000$, who report values of $\Gamma^* \sim 2.5$ to 3 for a stationary body. The most striking feature of the circulation plot, for the vibrating body, is the remarkably constant circulation value of the stronger vortex at $\Gamma^* \approx 2.85$, along the whole synchronization regime. The strength of the weaker vortex is $\Gamma^* \approx 0.6$ for the upper branch, representing only about 20% of the circulation of the stronger vortex. In the lower branch, the weaker vortex strength increases slowly as U^* is increased, but ultimately only reaches $\Gamma^* \approx 1.7$, representing about 60% of the stronger vortex circulation. The corresponding total shed circulation per half-cycle, towards the end of the lower branch, increases to $\Gamma^* \approx 4.5$, nearly 200% of the value for the stationary cylinder case.

5.2. *High-mass–damping type of response*

A comparison is now made of the near-wake vorticity dynamics for the two different response branches, in the case of high mass–damping. The three vorticity plots in figure 16 are taken when the body has reached its lowest point of the oscillation, but correspond to different points marked as the 'bull's eye' data points in the amplitude response plot of figure 8. Case (*a*) is for a point midway up the initial branch, case (*b*) is for the maximum amplitude point at the top of the initial branch, and case (*c*) is taken for the lower branch. These vorticity plots indicate that along the whole of the initial branch, there is a 2S mode of vortex formation; there is no deformation and splitting to cause the 2P mode, and the initial branch is continuous. On the other hand, the process of vortex deformation and splitting, in a manner seen in the previous section, does occur for the lower branch in (*c*). There is again a good correspondence between the switch in timing of vortex shedding (compare (*a*) and (*c*)), and the fact that the phase of the vortex force, ϕ_{vortex}, jumps by about 140° across the initial ↔ lower transition.

6. Frequency response

It is known from the work of Griffin & Ramberg (1982) and Khalak & Williamson (1999) that a reduction of mass ratio can increase the regime of velocity U^* over

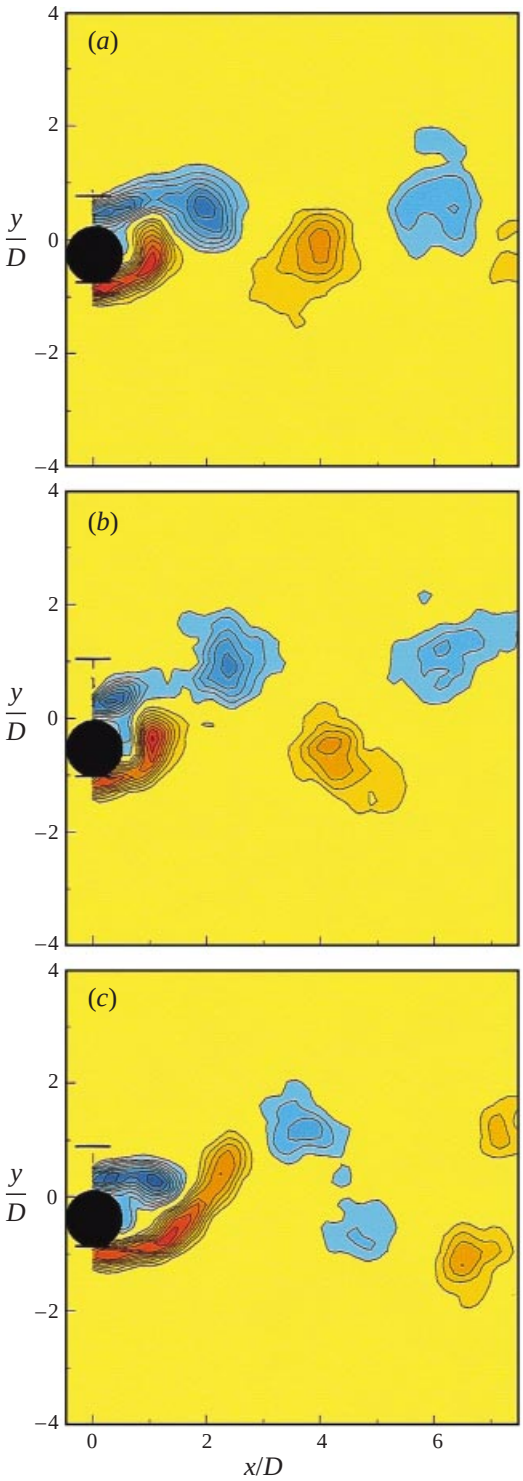

FIGURE 16. Wake formation modes for high $m^*\zeta$. Here we show the 2S ↔ 2P mode change at the initial ↔ lower transition. These cases correspond to data points marked as ⊙ in the amplitude response plot in figure 8(*a*). Contour levels are as in figure 11. (*a*) Initial branch – 2S mode ($A^* = 0.26$); (*b*) initial branch – 2S mode ($A^* = 0.52$); (*c*) lower branch – 2P-mode ($A^* = 0.42$).

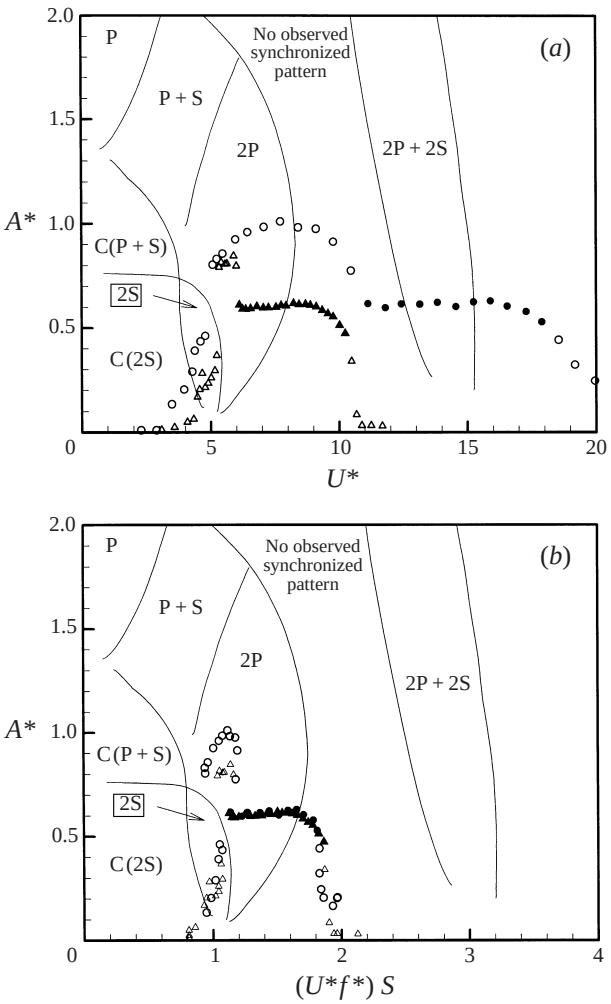

FIGURE 17. Amplitude response for two different mass ratios (m^*) plotted in the Williamson–Roshko (1988) map of wake modes. In (*b*), the lower-branch regimes collapse well when plotted against a different normalized velocity $(U^*/f^*)S$, as discussed in Khalak & Williamson (1999). ●, ○, $m^* = 1.19$ and $(m^* + C_A)\zeta = 0.0110$; ▲, △, $m^* = 8.63$ and $(m^* + C_A)\zeta = 0.0145$. Solid symbols indicate the lower-branch regimes.

which there is synchronization. In this section, all the responses will be of the low-mass–damping type (for $(m^* + C_A)\zeta < 0.05$), exhibiting three response branches. We shall show that reduction of m^* to $O(1)$ can yield a synchronization regime that is in excess of twice the largest regime we have shown to this point. We shall derive simple quantitative expressions for the oscillation frequency, f^*, in the lower branch, which permits us to obtain a relation for the regime of synchronization as a function of mass ratio, m^*. *These functional relations will show that there exists a critical mass ratio, below which the synchronization regime extends to infinity.*

Comparison of the extent of the synchronization regime for two mass ratios may be seen in figure 17. At moderate mass ratios ($m^* = 8.63$), the synchronization regime extends to about $U^* \approx 10$. When mass ratio is decreased to $m^* = 1.19$, this regime experiences a significant increase, reaching $U^* \approx 18$. However, when the two response

data sets are plotted versus the parameter $(U^*/f^*)S$, which is equivalent to (f_{vo}/f) (or the inverse of the ratio of actual oscillating frequency to the fixed-body shedding frequency), then the data sets collapse very well. Such a collapse of free-vibration data using this velocity parameter was first made in Khalak & Williamson (1999), and it was shown that this result cannot *a priori* be predicted. Since the case of lower mass ratio here also has a lower mass–damping, the peak amplitude in the upper branch is increased, while the lower-branch data sets collapse well. Of importance in this section, *the lower-branch amplitude levels are nearly independent of mass ratio,* m^*, so long as $(m^* + C_A)\zeta$ is small. This is consistent with the Griffin plot results in figure 2, which show that for $(m^* + C_A)\zeta < 0.05$, the lower-branch amplitudes remain (to reasonable accuracy) at a constant level.

6.1. *Lower-branch frequency and the existence of a critical mass ratio* (m^*_{crit})

In this section, we are interested principally in the frequency response, and in possible means to predict the frequency. Returning to the case of $m^* = 1.19$, now plotted in figure 18, the lower-branch frequency is remarkably constant for the complete regime of synchronization (and is substantially higher than for our $m^* = 8.63$ case earlier) with a value of $f^*_{lower} \approx 1.8$. A similar constant level of frequency in the lower-branch regime is shown for three different values of m^* in figure 19. This is a general characteristic of the lower-branch regime for low mass–damping. This is also supported by the frequency data of Hover *et al.* (1998) and Khalak & Williamson (1999), both under comparable low-mass–damping conditions.

A large set of data for the lower-branch frequency (f^*_{lower}) plotted versus m^* is shown in figure 20. These data are from our own experiments, and from Hover *et al.* (1998), Khalak & Williamson (1999), and Anand (1985). The data collapse very well onto a single curve. We would like now to deduce a functional relationship, for low mass–damping (broadly $(m^* + C_A)\zeta < 0.05$), as follows:

$$f^*_{lower} = \text{function}\,\{m^*\}.$$

Since the response in the lower-branch regime is remarkably sinusoidal and periodic (see for example Appendix B), the assumed equations of motion (1.1)–(1.3) are an excellent representation of the dynamics. Therefore the equation for frequency will take the form of equation (1.5), which we recall is

$$f^* = \sqrt{\frac{(m^* + C_A)}{(m^* + C_{EA})}}.$$

The effective added mass (C_{EA}) is a function of $\{(U^*/f^*)S, A^*\}$, and will have a unique value at each point along the lower branch, when plotted in the plane $\{(U^*/f^*)S, A^*\}$ as in figure 17(*b*). Since all lower-branch data sets will lie nearly along the same line in this figure, almost independently of mass ratio, m^*, then the value of C_{EA} along this line will be independent of m^*. For a given value of m^*, along the lower branch f^* is almost constant, as we observed in figure 19. This means from equation (1.5) that C_{EA} is constant along the lower branch. Now if $C_{EA} =$ constant for one set of data at a given m^*, then it will be the same constant value for all other m^*. We continue to assume here that mass–damping is small.

We now seek the value of C_{EA} that is a constant all along the lower-branch regime and is independent of m^*. To find this value, we find the best fit of C_{EA} in equation (1.5) which represents the experimental data of figure 20. From this analysis, we find to experimental accuracy $C_{EA} = -0.54 \pm 0.02$, and we thereby deduce the following

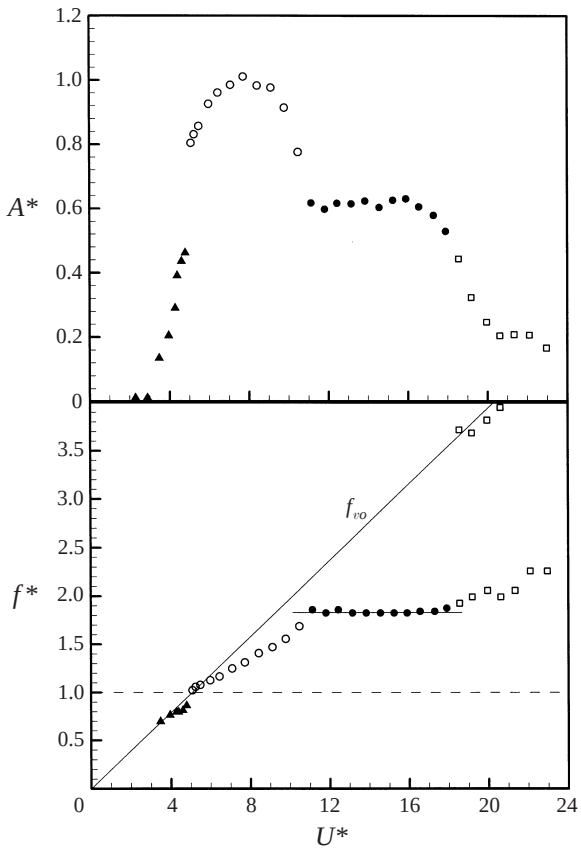

FIGURE 18. Amplitude and frequency response as a function of normalized velocity, U^*, for very low mass ratio, $m^* = 1.19$. The maximum frequency response in the synchronized regime, and the end of synchronization, are both considerably higher at this low m^*, compared to the $m^* = 8.63$ case in figure 3. ▲, Initial; ○, upper; ●, lower; □, desynchronized regime. Case of low $m^*\zeta$ and for $\zeta = 0.00502$.

lower-branch frequency equation:

$$f^*_{lower} = \sqrt{\frac{(m^* + C_A)}{(m^* - 0.54)}}, \tag{6.1}$$

where $C_A = 1.0$. This curve is drawn through the data in figure 20, and it represents the data very well. It should be said that our deduced value for C_{EA} is consistent with results from forced oscillations by Gopalkrishnan (1993), where he finds $C_{EA} \approx -0.60$ in a large region of the $\{A^*$ versus $(U^*/f^*)S\}$ plane, encompassing the complete domain of the lower branch. The expression for f^*_{lower} in equation (6.1) provides a practical and simple means to calculate the highest frequency in the synchronization regime, if we are given the mass ratio, m^*.

An important consequence of equation (6.1) is that the frequency becomes large as the mass ratio reduces to a limiting value of 0.54. Therefore we conclude that there exists a critical mass ratio:

$$m^*_{crit} = 0.54.$$

The existence of a critical mass is, for us, a surprising and interesting result.

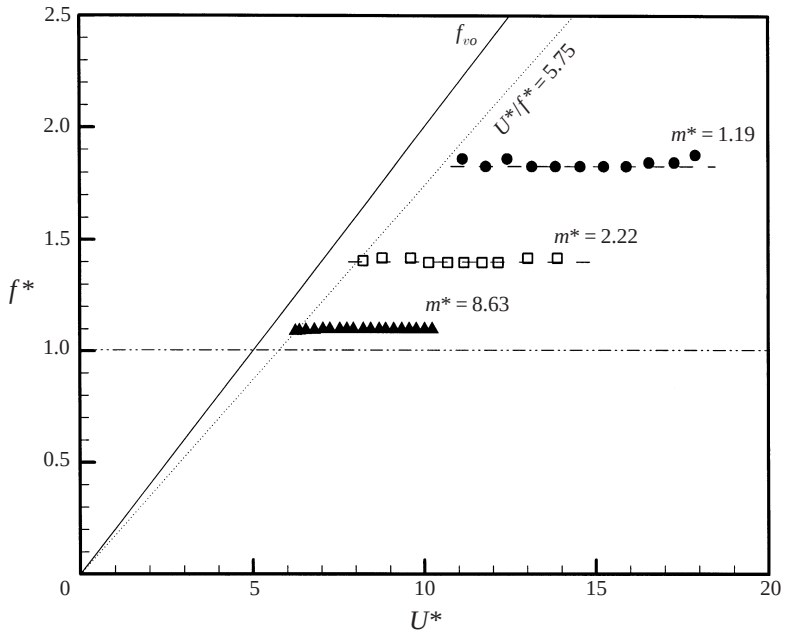

FIGURE 19. Lower-branch frequency response for different mass ratios, showing a nearly constant value for each specific m^*. Case of low $m^*\zeta$.

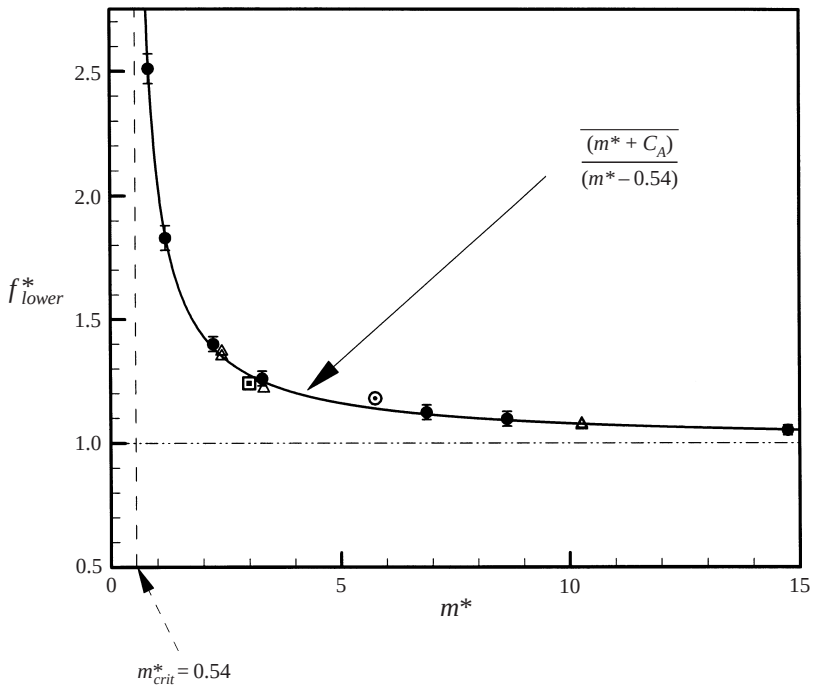

FIGURE 20. Variation of the lower-branch frequency (f^*_{lower}) as a function of the mass ratio m^*. The equation for f^*_{lower} fits the data remarkably well, and indicates a dramatic increase in f^*_{lower} as we approach the critical mass ratio, $m^*_{crit} = 0.54$. ●, Present data; △, Khalak & Williamson (1999); ⊡, Hover *et al.* (1998); ⊙, Anand (1985).

As the mass ratio decreases, the value of normalized velocity, defining the start of the lower branch, increases according to the following relation (see figure 19):

$$\left(\frac{U^*}{f^*}\right)_{start} = 5.75. \tag{6.2}$$

(The experimental accuracy associated with the numerical values in (6.2) and (6.4) is within ± 0.2.) This is consistent with the start of the lower branch in the Williamson–Roshko (1988) map of regimes in figure 17(*b*), given by $(U^*/f^*)S \approx 1.14$, which (for $S = 0.20$) yields $(U^*/f^*) = 5.7$. Combining equations (6.1) and (6.2), we find the velocity defining the start of the lower branch:

$$U^*_{start} \approx 5.75\sqrt{\frac{(m^* + C_A)}{(m^* - 0.54)}}. \tag{6.3}$$

This shows that

$$U^*_{start} \to \infty \quad \text{as} \quad m^* \to m^*_{crit}.$$

Therefore, when mass ratios fall below $m^*_{crit} = 0.54$, the lower branch cannot be reached and ceases to exist. We conclude that the upper branch will continue indefinitely, and the synchronization regime will extend to infinity!

For conditions when the mass ratio is above critical, $m^* > m^*_{crit}$, we may also predict the velocity U^* defining the end of the lower branch in a manner similar to the above simple analysis, to give

$$\left(\frac{U^*}{f^*}\right)_{end} = 9.25, \tag{6.4}$$

giving an equation for U^*_{end} as

$$U^*_{end} \approx 9.25\sqrt{\frac{(m^* + C_A)}{(m^* - 0.54)}}. \tag{6.5}$$

The above expression yields a quantitative measure of the extent of the synchronization regime, for a given mass ratio, m^*. As discussed before, the regime becomes infinitely large when mass ratio falls below the critical value of 0.54. The extent of the complete synchronization regime, as a function of mass ratio, m^*, is shown as the shaded region in figure 21. The data marking the end of the synchronization (U^*_{end}) is represented well by equation (6.5). The plot includes data from Anand (1985), Hover *et al.* (1998), and Khalak & Williamson (1999).

6.2. *Upper-branch frequency*

We are interested here in the frequency (f^*) of the upper branch, and the upper–lower transition. For moderate mass ratios, $m^* = 8.63$, one may analyse the upper–lower transition using the Hilbert transform (following Khalak & Williamson 1997, 1999) to determine an instantaneous frequency, as shown for example at $U^* = 5.85$ in the lower time traces of figure 22(*a*). From such examples, one may build up a complete set of frequency data for the upper and lower branches, where they overlap, as seen in the upper plot of figure 22(*a*). In essence, both frequencies may be determined in the upper $\leftrightarrow$ lower transition at $m^* = O(10)$.

On the other hand, as mass ratio is reduced to $m^* = 1.19$ in figure 22(*b*), the time scale of switching frequencies is much smaller, and it becomes unclear whether one is actually switching between two distinct frequencies (i.e. between distinct response

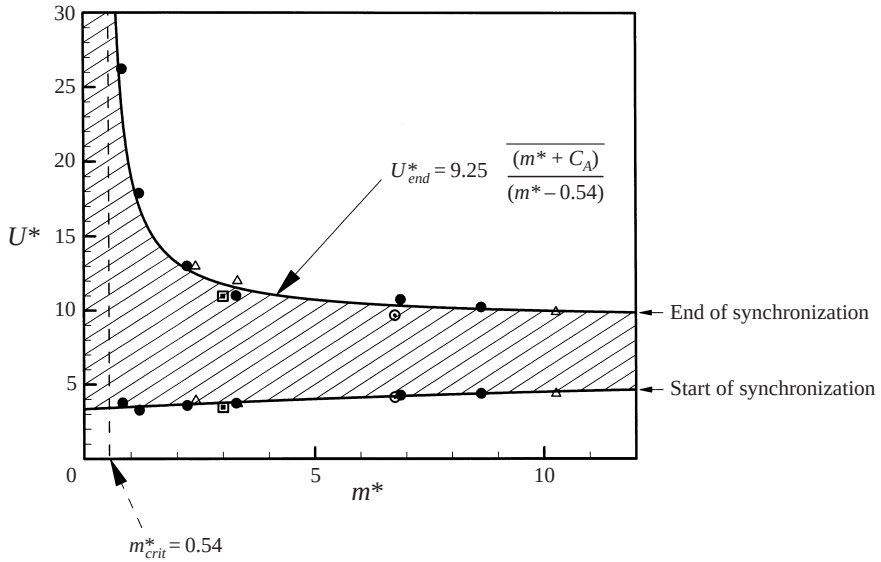

FIGURE 21. The extent of synchronization (shaded region) as a function of mass ratio, m^*. The equation for U^*_{end} fits the data well, and indicates a dramatic increase in the extent of the synchronization regime, determined by U^*_{end}, as we approach the critical mass ratio, $m^*_{crit} = 0.54$. For $m^* < m^*_{crit}$, the range of synchronization will extend to infinity. Symbols are as in figure 20.

branches) anymore. From analysis of spectral peaks, it appears that the frequency f^* travels along a line from a point close to $U^* = 5.0$ and $f^* \approx 1.0$, to the point marking the start of the lower branch. This characteristic frequency variation was found for several other different mass ratios of the same order, $m^* = O(1)$. As m^* becomes smaller, one would expect a gradual departure from the mode switching of case (*a*) at $m^* = O(10)$, to the apparently 'linear' variation of frequency of case (*b*) at $m^* = O(1)$.

If we reduce mass ratio, m^* below the critical value, i.e. $m^* < 0.54$, then we expect the upper branch to continue indefinitely. By setting $m^* = 0.52$, in figure 23, we note that the regime of synchronization is huge compared even to the $m^* = 8.63$ case. The regime extends far beyond $U^* = 22$, but could not be captured due to the experimental limits of our facility. The cylinder oscillations, even at these high U^*, continue to be nearly periodic as shown by time traces of the oscillations in figure 23. The oscillation frequency f^* increases almost 'linearly', as for $m^* = 1.19$, although in this case we pass through $f^* = 4$, before the limits of our facility are reached. In other words, the body oscillates at large amplitude, at a frequency which is four times the natural frequency of the structure in water! Note that the frequency data lie along a straight line, with a slope of close to 0.174 or $1/(5.75)$. The line does not pass through the origin, but instead has a positive intercept on the y-axis. We may understand this feature better, by looking now at figure 24.

A schematic diagram of frequency response at different mass ratios is given in figure 24. Over a large range of mass ratios, the start of the upper branch is found to be close to the point marked as ①, where $U^* \approx 1/S \approx 5.0$; and where $f^* \approx 1.0$. The upper-branch frequencies are represented, in this diagram, as falling on a straight line from this point, up to the point where the lower branch begins. The start of the lower branch satisfies the condition in equation (6.2):

$$\left(\frac{U^*}{f^*}\right)_{start} = 5.75,$$

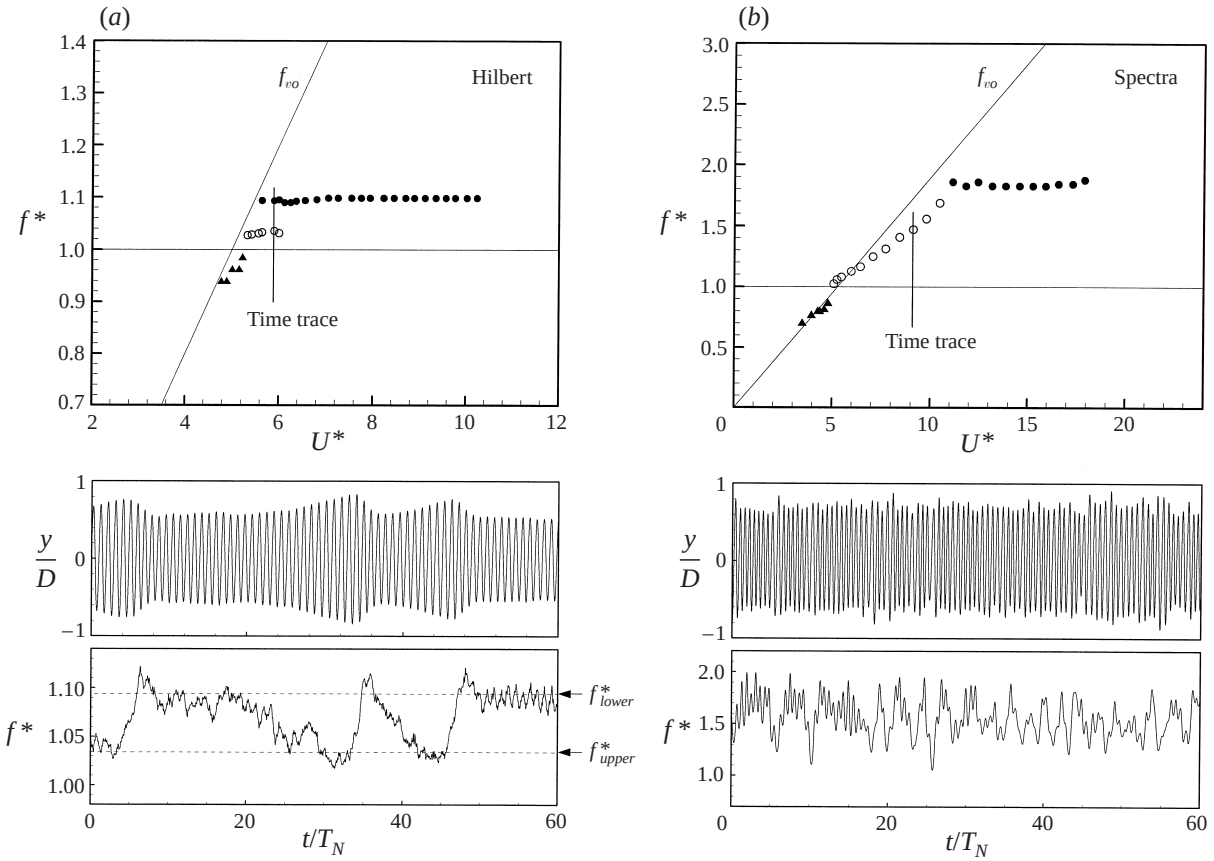

FIGURE 22. Frequency response (f^*) for two mass ratios, showing especially the character of the frequency in the upper ↔ lower transition: (*a*) $m^* = 8.63$, (*b*) $m^* = 1.19$. In the lower two plots, we show time traces of the frequency f^* (using Hilbert transform) and displacement. These figures show intermittent switching between the modes in (*a*), which permits estimation of the frequencies of the upper and lower branch parts separately. In (*b*), the frequency and amplitude vary more rapidly, and it is not possible to interpret two distinct frequencies from this analysis. The damping ratios are (*a*) $\zeta = 0.00151$, (*b*) $\zeta = 0.000502$.

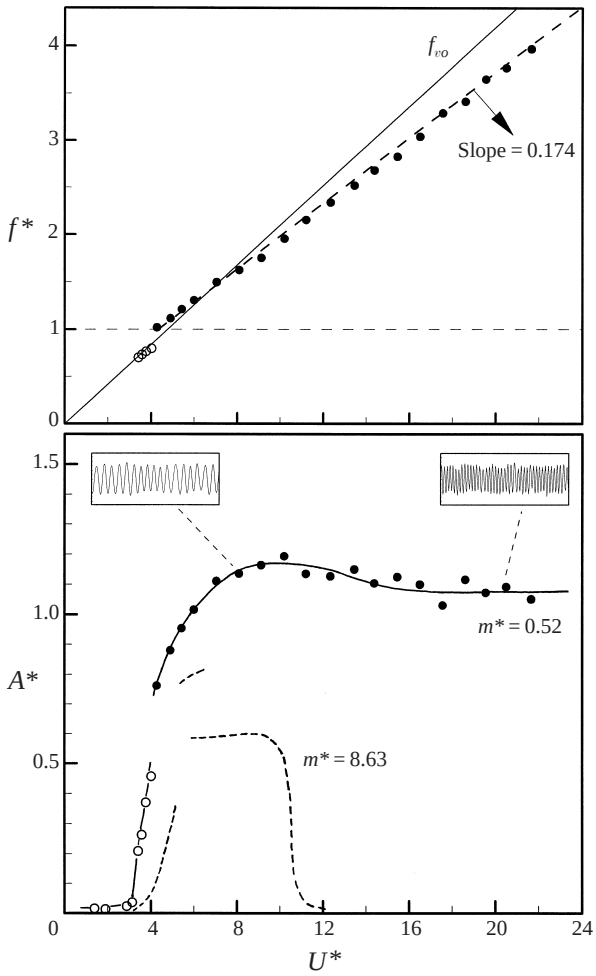

FIGURE 23. Response character when the mass ratio falls below the critical value, $m^* = 0.52$. The upper branch persists beyond the limits of our facility ($U^* \sim 20$). The corresponding frequency lies along a straight line, with a slope of 0.174, which is predicted from our equation (6.2). The mass ratio $m^* = 0.52$, and $\zeta = 0.0052$.

and is shown as one of the two dotted lines in the figure. For a given mass ratio (m^*), the start of the lower branch will be defined, along this line, where the frequency f^* becomes f^*_{lower} given by equation (6.1):

$$f^*_{lower} = \sqrt{\frac{(m^* + C_A)}{(m^* - 0.54)}},$$

which in the case of $m^* = 1.05$, for example, is marked as point ②. Then the lower-branch frequency remains constant until it reaches point ③ situated on the other dotted line defining the end of the lower branch, given by equation (6.4):

$$\left(\frac{U^*}{f^*}\right)_{end} = 9.25.$$

As the mass ratio approaches $m^* = 0.54$, the point along the line $(U^*/f^*) = 5.75$

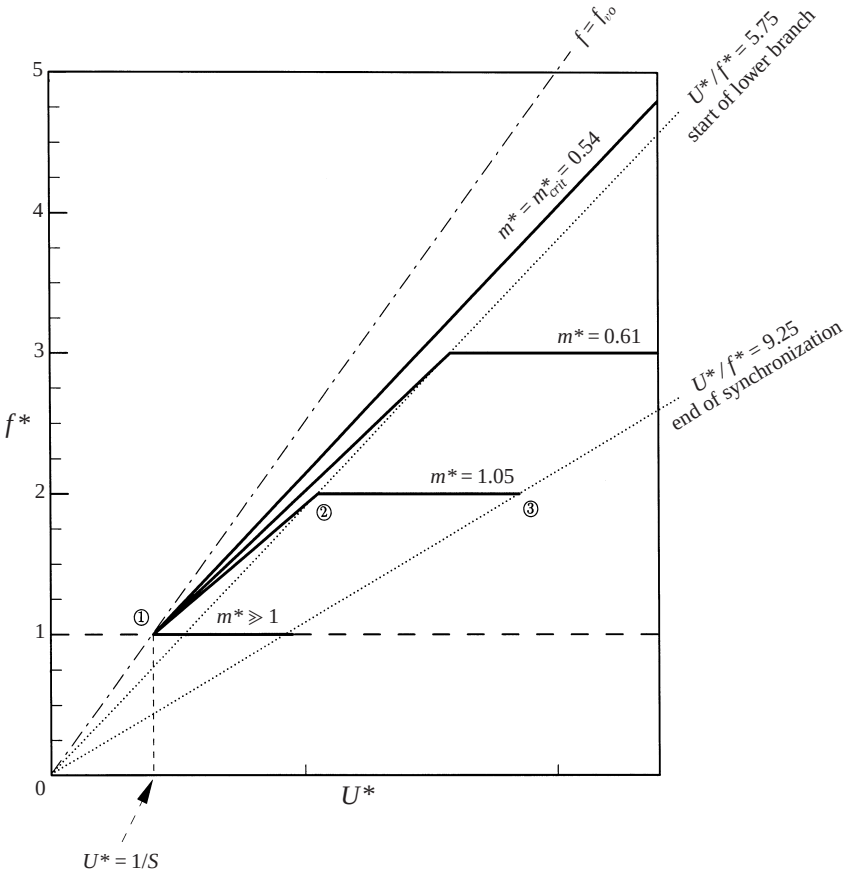

FIGURE 24. Schematic plot of the frequency response for different mass ratios, under conditions of low ($m^*\zeta$). The frequency in the lower branch remains constant for each m^*. The conditions indicating the start of the lower branch, and the end of synchronization regime, from equations (6.2) and (6.5), are also shown.

where the lower branch begins will correspond with a frequency f^* which tends to infinity. Under these conditions, the upper-branch frequencies will lie along a line which is parallel to $(U^*/f^*) = 5.75$ but shifted to the left by $(\Delta U^* = 0.75)$. The slope is 0.174, and corresponds with the upper-branch line defining f^* found from experimental measurements in figure 23. This now explains why the frequency line in figure 24 does not pass through the origin, and instead has some intercept on the y-axis. The summarizing diagram in figure 24 also explains why the slope of the upper-branch frequency line will always be lower than the slope defining the Strouhal frequency line, $f = f_{vo}$.

6.3. *Overview of the effect of mass ratio on response*

The broad effects of varying mass ratio on response can be seen in figure 25 where we have pairs of amplitude and frequency plots for quite similar mass–damping ($(m^* + C_A)\zeta \approx 0.01$) in all three pairs of plots, so that peak amplitudes are similar. As mass ratio is decreased, the figure shows a large increase in the range of synchronization for both the upper and lower branches. This is made especially clear in this

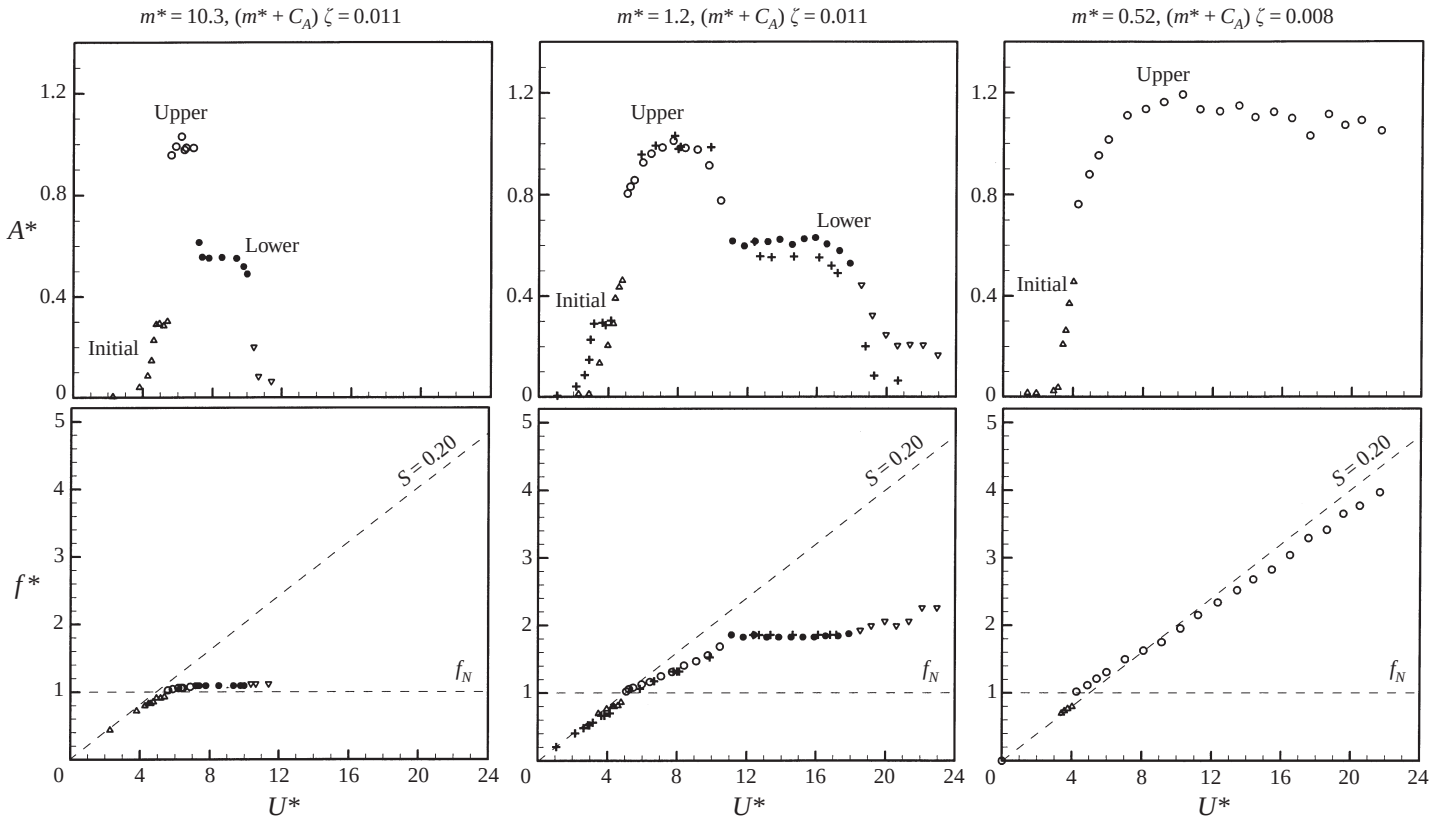

FIGURE 25. Pairs of amplitude–frequency plots for decreasing mass ratio (m^*), plotted to the same scale. A large increase in upper/lower frequency (f^*), and in the range of synchronization can be clearly observed as m^* is reduced. The mass–damping parameter $[(m^* + C_A)\zeta]$ for all three cases shown is approximately 0.01. △, Initial; ○, upper; ●, lower; ▽, desynchronized regime; +, predicted $m^* = 1.2$ response from $m^* = 10.3$ response data.

presentation, where all the plots are to the same scale. The corresponding frequency levels dramatically increase, as m^* is reduced.

It is worth noting that one may approximately predict these kinds of response from a single set of amplitude–frequency data, if we assume that, for similar mass–damping ($m^*\zeta$), the amplitude response plots all collapse onto the same locus of points in the plane A^* versus (U^*/f^*). (Although this point is not known *a priori*, the results of Khalak & Williamson (1999), and figure 17 in this paper, show this assumption to be very good, under a wide range of conditions.) From such a collapsed response plot, combined with a knowledge of C_{EA} computed at all points along this locus of points, we can very simply predict the amplitude and frequency response, for any mass ratio. A typical example of such a prediction, using the data at $m^* = 10.3$ to compute the response for $m^* = 1.2$ is shown as the crosses (+) in figure 25. The agreement in amplitude is good, while the agreement in frequency is excellent. (C_{EA} is deduced simply from a rearrangement of equation (1.5), as follows: $C_{EA} = (m^* + C_A)/(f^*)^2 - m^*$. Since C_{EA} is known, one can compute the frequency response using the equation: $f^* = [(m^* + C_A)/(m^* + C_{EA})]^{(1/2)}$, for any value of mass ratio, m^*. This then yields the amplitude response A^* as a function of U^*.)

In conclusion, the central purpose of this overview figure is to encapsulate the effects of mass ratio on amplitude and frequency response, indicating with some clarity the departure from the classical synchronization phenomena, as mass ratio becomes very small.

7. Conclusions

In this work, we investigate the transverse vortex-induced vibrations of an elastically mounted rigid cylinder in a fluid flow, where we have the capability to reduce mass and damping to very low levels. We employ the DPIV technique to determine the vorticity field, simultaneously with force and displacement measurements, for the first time in such a free-vibration study.

There exist two distinct types of response in such systems, depending on whether one has a high or low combined mass–damping parameter ($m^*\zeta$). In the high-($m^*\zeta$) case, one finds two response amplitude modes, which we define here as the initial and lower branches. Across the mode transition, a jump in amplitude and in phase angle (between force and displacement) is observed, as normalized velocity (U^*) is increased. In the case of low ($m^*\zeta$), as found by Khalak & Williamson (1996, 1999), there exist three branches of response, namely the initial, upper and lower branches. Since there are three branches in this case, there exist two mode transitions.

In order to understand the existence of two mode transitions for low ($m^*\zeta$), we employ two formulations of the equation of motion, one of which uses the 'total force', while the other uses the 'vortex force', which is related only to the dynamics of vorticity. The latter formulation is particularly useful in that the 'vortex phase' (between vortex force and displacement), ϕ_{vortex}, is usefully indicative of the mode of vortex formation. We therefore define two distinct phases, as follows:

$$\text{'VORTEX PHASE'} = \phi_{vortex} = \text{Phase between VORTEX force and displacement,}$$

$$\text{'TOTAL PHASE'} = \phi_{total} = \text{Phase between TOTAL force and displacement.}$$

The first mode jump at the initial–upper branch transition, involves a large jump in 'vortex phase', ϕ_{vortex}. This is associated with a jump between 2S and 2P vortex wake modes (as defined in Williamson & Roshko 1988). There is thus a corresponding

switch in vortex shedding timing. At this mode jump, the frequency of oscillation (f) passes through the natural frequency of the system in the fluid ($f_{N\,water}$).

Across the second mode jump at the upper–lower transition, there is a jump in 'total phase', ϕ_{total}. However, in this case, there is no jump in ϕ_{vortex}, since both branches are associated with the 2P mode. This jump in classical phase does not reflect a switch in timing of vortex shedding, contrary to previous assumptions in the literature. At this mode jump, the frequency of oscillation (f) passes through the natural frequency *in vacuo* ($f_{N\,vacuum}$).

In the case of high ($m^*\zeta$), the vibration frequency jumps across both $f_{N\,water}$ and $f_{N\,vacuum}$ at the same velocity U^*. Therefore, the jumps in ϕ_{vortex} and ϕ_{total} occur simultaneously, yielding only one mode transition, and two response branches. Under these conditions, the switch in the timing of vortex shedding is indeed coincident with the phase jump (ϕ_{total}), which is in agreement with previous assumptions.

At high mass ratios, $m^* = O(100)$, one expects from classical work that the frequency ratio (f^*), (vibration frequency/natural frequency), will be close to 1.0. However, for very low mass ratios, $m^* = O(1)$, the vibration frequency during synchronization increases dramatically, $f^* \gg 1$. By using the equation of motion, and observing the nature of the response amplitude and frequency for the lower branch, we deduce an expression for the frequency of the lower-branch vibration, valid in the case of low ($m^*\zeta$), as follows:

$$f^*_{lower} = \sqrt{\frac{(m^* + C_A)}{(m^* - 0.54)}},$$

which agrees very well with a wide set of experimental data. This frequency equation indicates the existence of a critical mass ratio, when f^* becomes large:

$$m^*_{crit} = 0.54.$$

Also, by deducing an expression defining the start of the lower branch,

$$U^*_{start} \approx 5.75\sqrt{\frac{(m^* + C_A)}{(m^* - 0.54)}},$$

we see that, for $m^* < m^*_{crit}$, the lower branch can never be reached and ceases to exist. In this case, the upper-branch regime of synchronization will continue indefinitely. Experiments at $m^* < m^*_{crit}$ show the beginnings of this high-amplitude upper branch, persisting to the limits of our facility, and yielding vibration frequencies in excess of 4 times the natural frequency.

Further studies have been made of the vortex wake modes. In particular, there has been some debate in the literature as to whether the 2P mode is a steady-state periodic vortex wake mode. Our DPIV, force and displacement measurements show that this 2P mode is a steady-state mode, and is highly repeatable. The formation of two same-sign vortices in each half-cycle of the 2P mode is associated with the stretching and splitting of each vortex, which itself is related to the intense strain rate field of neighbouring vortices. These strain regions fall inside the developing vorticity concentrations for the 2P mode, hence we see the splitting and formation of vortex pairs. For the 2S mode, the intense strain region falls outside the developing vortices, hence the vortices are not split.

The support from the Ocean Engineering Division of ONR, monitored by Dr

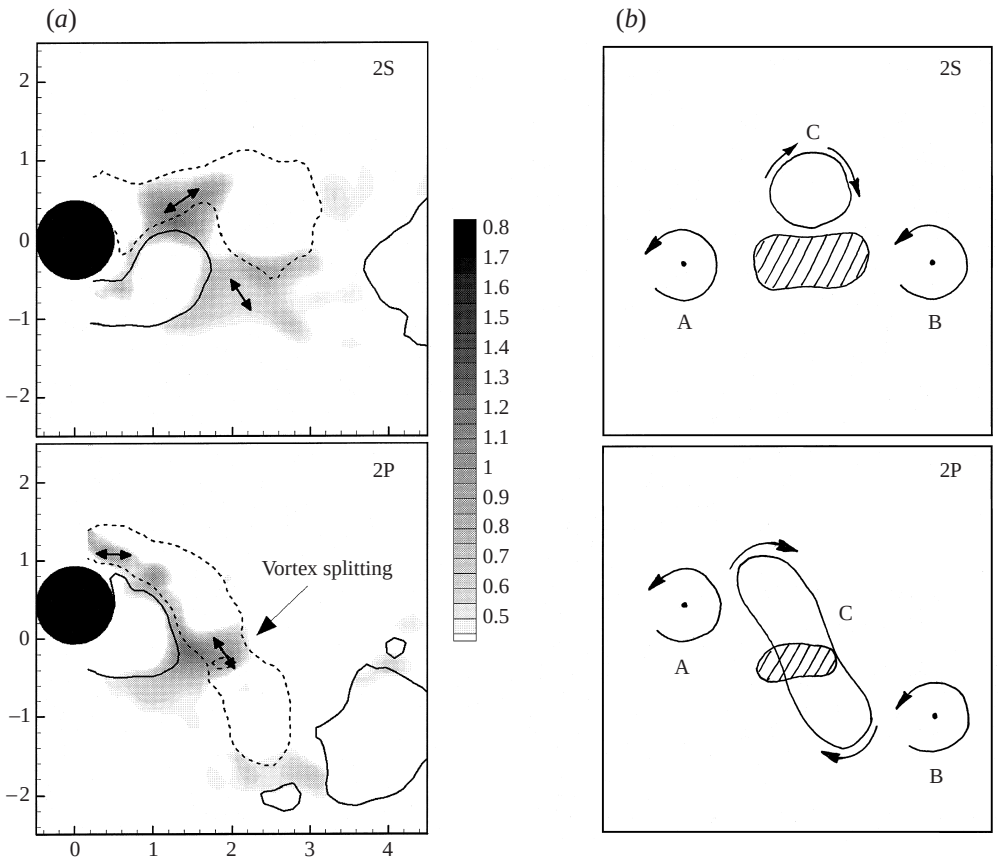

FIGURE 26. Strain rate levels calculated from DPIV measurements in (*a*), and a schematic of the principal strain rate regions in (*b*), corresponding to the 2S mode (of the initial branch) and the 2P mode (of the lower branch). In the 2P mode, the high strain rate region is located within the primary vorticity concentration C, whereas for the 2S mode it lies outside the main regions of vorticity concentration. Arrows indicate the principal stretching direction in the high strain rate regions. Strain rate levels shown in (*a*) are non-dimensional ($\varepsilon D/U$).

Tom Swean, is gratefully acknowledged (ONR Contract Nos. N00014-94-1-1197 and N00014-95-1-0332).

Appendix A. Vortex splitting as a mechanism causing the 2P mode

The formation of the 2P mode is associated with a splitting of a region of vorticity each half-cycle, as observed in the sequence of figure 13. On the other hand, the 2S mode comprises vorticity concentrations that apparently do not split in two in each half-cycle. We can understand this tendency to split, or not to split, by briefly studying the strain rate field in the vortex formation region behind the oscillating body, in figure 26, computed from the velocity field using DPIV. In the case of the 2S mode, a high strain rate region exists between the two anticlockwise vortices, A and B, but the formation of vortices is such that the clockwise vortex C lies above this intense strain rate region. On the other hand, in the case of the 2P mode, the intense strain rate region lying between vortices A and B now is situated over the centre of the evolving and deforming vortex C, which is then split apart to form two separate vortices (and

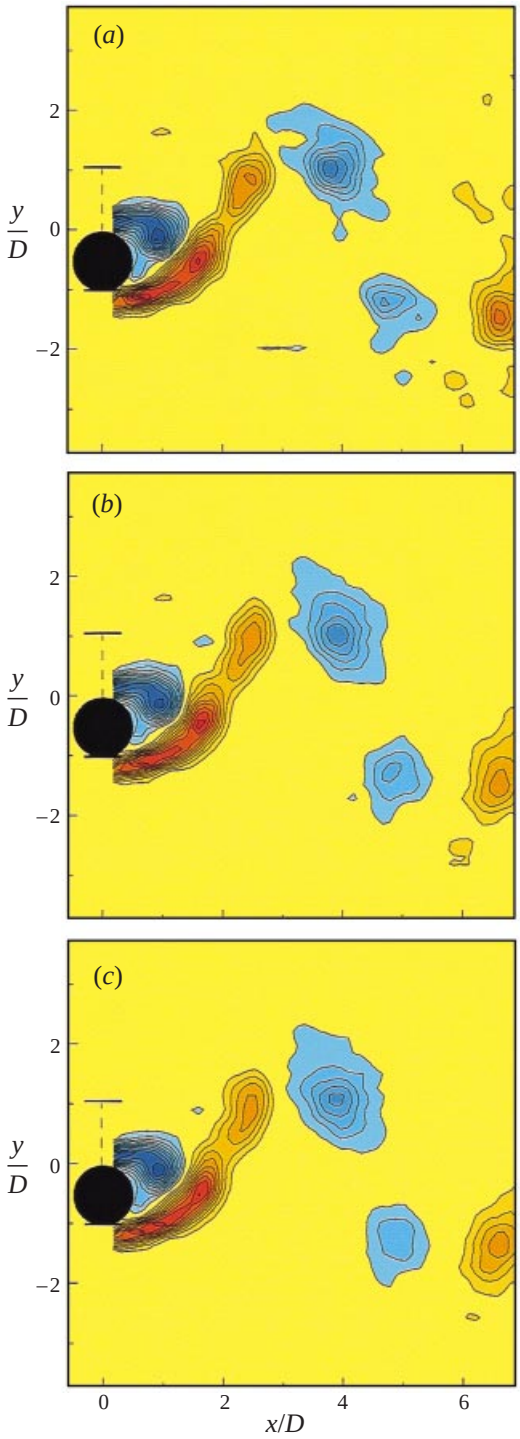

FIGURE 27. Vorticity contours for the 2P mode, averaged over (*a*) 5, (*b*) 10 and (*c*) 20 randomly chosen cycles. The cylinder is at the bottom extreme position in all three cases. Contour levels shown are $\omega D/U = \pm 0.4, \pm 0.8, \pm 1.2, \ldots$ ($U^* = 6, 4$, $A^* \approx 0.6$, $Re \approx 3700$).

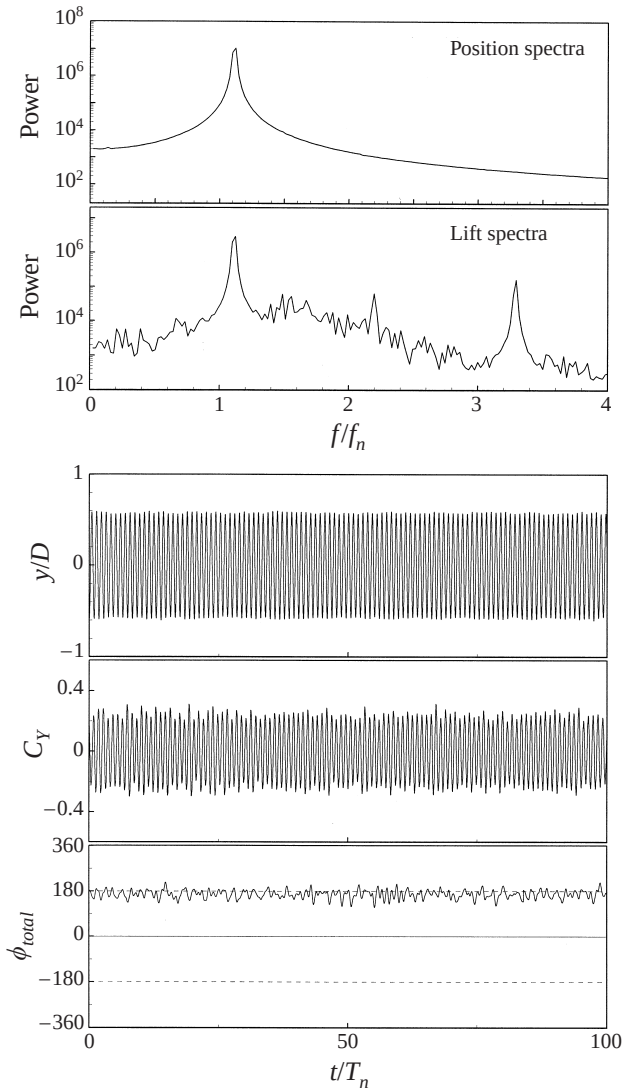

FIGURE 28. Spectra and time traces of the force and displacement for the 2P mode, corresponding to the vorticity contours in figure 27, showing that the response is steady state and highly periodic. In addition, the 'total phase' (ϕ_{total}) is reasonably constant at just below 180° indicating that there is no change in the shedding mode (which would be associated with a jump of around 180°).

thus to form into the vortex pair pattern). The directions of principal stretching, marked by arrows, are consistent with the deformation and splitting of vortex C. These scenarios are shown schematically in figure 26(*b*). The main point to note here is that the high strain rate region between neighbouring vortices lies within a vorticity concentration for the 2P mode, unlike the case of the 2S mode. The deformation and vortex splitting process appears to be fundamental to the 2P wake formation mode.

Appendix B. Repeatability of the 2P mode

There has been some debate concerning both numerical simulation and experiment about the existence of the 2P mode. We shall present evidence briefly here, which

indicates that the 2P mode of the lower branch (we choose here $m^* = 8.63$, $\zeta = 0.0015$, $U^* = 6.4$, $A^* = 0.6$, $Re \approx 3700$) is highly repeatable, and continues indefinitely in our study.

In order to demonstrate that the 2P mode is repeatable, we conducted a study with the experiment running continuously between noon and dinner time, corresponding to about 10 000 oscillation cycles. Within this large time period, we captured at random periods (and one at a time) a large number of DPIV vorticity contours at the same phase of the body motion. Random sets of these vorticity plots were averaged, all of which clearly correspond to the 2P mode. Whether these sets comprised averages of 5, 10 or 20 (or more) random cycles, the main vortex locations and size are quite unaffected, as shown, for example, in figure 27. The corresponding spectra and time traces of the position and force, shown in figure 28, demonstrate that the response is highly periodic. In addition, the phase ϕ_{total} is reasonably constant at just below 180°. Any change in the shedding mode back to the upper-branch 2P mode, or to the 2S mode, would indicate a jump in ϕ_{total} by around 180°, which was never observed during the time span of the experiment.

We feel that, since the 2P mode was observed for in excess of 10 000 cycles, it might not be rash to suggest that the 2P mode is a steady-state periodic wake mode.

REFERENCES

Adrian, R. J. 1991 Particle imaging techniques for experimental fluid mechanics. *Ann. Rev. Fluid Mech.* **23**, 261–304.

Anagnostopoulos, P. & Bearman, P. W. 1992 Response characteristics of a vortex-excited cylinder at low Reynolds numbers. *J. Fluids Struct.* **6**, 39–50.

Anand, N. M. 1985 Free span vibrations of submarine pipelines in steady and wave flows. PhD thesis, Norwegian Institue of Technology, Trondheim, Norway.

Atsavapranee, P., Voorhees, A. V., Benaroya, H. & Wei, T. 1998 'Reverse' lock-in regime on a freely oscillating cylinder. *Bull. Am. Phys. Soc.* **43**, 2045.

Balasubramanian, S. & Skop, R. A. 1996 A nonlinear oscillator model for vortex shedding from cylinders and cones in uniform and shear flows. *J. Fluids Struct.* **10**, 197–214.

Bearman, P. W. 1984 Vortex shedding from oscillating bluff bodies. *Ann. Rev. Fluid Mech.* **16**, 195–222.

Bearman, P. W. & Currie, I. G. 1979 Pressure-fluctuation measurements on an oscillating circular cylinder. *J. Fluid Mech.* **91**, 661–677.

Bishop, R. E. D. & Hassan, A. Y. 1964 The lift and drag forces on a circular cylinder oscillating in a flowing fluid. *Proc. R. Soc. Lond.* A **277**, 51–75.

Blackburn, H. M. & Henderson, R. D. 1995 Wake dynamics in flow past an oscillating cylinder. In *9th Conf. on Numerical Methods in Laminar and Turbulent Flow, Atlanta, GA, USA, July 1995.*

Blackburn, H. M. & Henderson, R. D. 1999 A study of two-dimensional flow past an oscillating cylinder. *J. Fluid Mech.* **385**, 255–286.

Blevins, R. D. 1990 *Flow-Induced Vibrations.* Van Nostrand Reinhold.

Brika, D. & Laneville, A. 1993 Vortex-induced vibrations of a long flexible circular cylinder *J. Fluid Mech.* **250**, 481–508.

Chyu, C. & Rockwell, D. 1996 Evolution of patterns of streamwise vorticity in the turbulent near wake of a circular cylinder. *J. Fluid Mech.* **320**, 117–137.

Evangelinos, C. & Karniadakis, G. E. 1999 Dynamics and flow structures in the turbulent wake of rigmd and flexible cylinders subject to vortex-induced vibrations. *J. Fluid Mech.* **400**, 91–124.

Feng, C. C. 1968 The measurements of vortex-induced effects in flow past a stationary and oscillating circular and D-section cylinders. Master's thesis, University of British Columbia, Vancouver, BC, Canada.

Fujarra, A. L. C., Meneghini, J. R., Pesce, C. P. & Parra, P. H. C. C. 1998 An investigation of vortex-induced vibration of a circular cylinder in water. In *Proc. BBVIV-1 Bluff Body*

Wakes and Vortex-Induced Vibrations, Washington, D.C., 21–23 June 1998 (ed. P. W. Bearman & C. H. K. Williamson). Paper number 25; also Paper FEDSM98-5195 in CD-ROM from ASME.

Gharib, M. R., Leonard, A., Gharib, M. & Roshko, A. 1998 The absence of lock-in and the role of mass ratio. In *Proc. BBVIV-1 Bluff Body Wakes and Vortex-Induced Vibrations, Washington, D.C., 21–23 June 1998* (ed. P. W. Bearman & C. H. K. Williamson). Paper Number 24; also Paper FEDSM98-5312 in CD-ROM from ASME.

Gopalkrishnan, R. 1993 Vortex-induced forces on oscillating bluff cylinders. PhD thesis, MIT.

Griffin, O. M. 1985 Vortex shedding from bluff bodies in a shear flow. *Trans. ASME*: *J. Fluids Engng* **107**, 298–306.

Griffin, O. M. & Ramberg, S. E. 1974 The vortex street wakes of vibrating cylinders. *J. Fluid Mech.* **66**, 553–576.

Griffin, O. M. & Ramberg, S. E. 1982 Some recent studies of vortex shedding with application to marine tubulars and risers. *Trans. ASME*: *J. Energy Resour. Techn.* **104**, 2–13.

Griffin, O. M., Skop, R. A. & Ramberg, S. E. 1975 The resonant vortex-excited vibrations of structures and cable systems. In *7th Offshore Technology Conf.* Houston, Texas, USA. OTC Paper 2319.

Gu, W., Chyu, C. & Rockwell, D. 1994 Timing of vortex formation from an oscillating cylinder. *Phys. Fluids* **6**, 3677–3682.

Hover, F. S., Techet, A. H. & Triantafyllou, M. S. 1998 Forces on oscillating uniform and tapered cylinders in crossflow. *J. Fluid Mech.* **363**, 97–114.

Jeon, D., Shan, J. & Gharib, M. 1995 Vorticity fields in the wake of an oscillating cylinder near the 'Critical Curve.' *Bull. Am. Phys. Soc.* **40**, 1996.

Khalak, A. & Williamson, C. H. K. 1996 Dynamics of a hydroelastic cylinder with very low mass and damping. *J. Fluids Struct.* **10**, 455–472.

Khalak, A. & Williamson, C. H. K. 1997 Fluid forces and dynamics of a hydroelastic structure with very low mass and damping. *J. Fluids Struct.* **11**, 973–982.

Khalak, A. & Williamson, C. H. K. 1999 Motions, forces and mode transitions in vortex-induced vibrations at low mass–damping. *J. Fluids Struct.* **13**, 813–851.

Lighthill, J. 1986 Wave loading on offshore structures. *J. Fluid Mech.* **173**, 667–681.

Lin, J.-C., Vorobieff, P. & Rockwell, D. 1995 3-dimensional patterns of streamwise vorticity in the turbulent near-wake of a cylinder. *J. Fluids Struct.* **9**, 231–234.

Lu, X.-Y. & Dalton, C. 1996 Calculation on the timing of vortex formation from an oscillating cylinder. *J. Fluids Struct.* **10**, 527–541.

Meneghini, J. R. & Bearman, P. W. 1995 Numerical simulation of high amplitude oscillatory flow about a circular cylinder. *J. Fluids Struct.* **9**, 435–455.

Moe, G. & Wu, Z.-J. 1990 The lift force on a cylinder vibrating in a current. *Trans. ASME*: *J. Offshore Mech. Arctic Engng* **112**, 297–303.

Naudascher, E. & Rockwell, D. 1994 *Flow-Induced Vibrations: An Engineering Guide*. Balkema.

Newman, D. J. & Karniadakis, G. E. 1997 Simulations of flow past a freely vibrating cable. *J. Fluid Mech.* **344**, 95–136.

Ongoren, A. & Rockwell, D. 1988 Flow structure from an oscillating cylinder. Part 2. Mode competition in the near wake. *J. Fluid Mech.* **191**, 225–245.

Parkinson, G. 1989 Phenomena and modelling of flow-induced vibrations of bluff bodies. *Prog. Aerospace Sci.* **26**, 169–224.

Pesce, C. P. & Fujarra, A. L. C. 2000 Vortex-induced vibrations and jump phenomenon: experiments with a clamped flexible cylinder in water. *Intl J. Offshore Polar Engng* **10**, 26–33.

Ramberg, S. E. & Griffin, O. M. 1981 Hydroelastic response of marine cables and risers. In *Hydrodynamics in Ocean Engineering*, pp. 1223–1245. Norwegian Institute of Technology, Trondheim, Norway.

Sarpkaya, T. 1978 Fluid forces on oscillating cylinders. *ASCE J. Waterway, Port, Coastal, Ocean Div.* **104**, 275–290.

Sarpkaya, T. 1979 Vortex-induced oscillations. *Trans. ASME*: *J. Appl Mech.* **46**, 241–258.

Sarpkaya, T. 1995 Hydrodynamic damping, flow-induced oscillations, and biharmonic response. *Trans. ASME*: *J. Offshore Mech. Arctic Engng* **117**, 232–238.

Sheridan, J., Carberry, J., Lin, J.-C. & Rockwell, D. 1998 On the near wake topology of an oscillating cylinder. *J. Fluids Struct.* **12**, 215–220.

Skop, R. A. & Balasubramanian, S. 1997 A new twist on an old model for vortex-excited vibrations. *J. Fluids Struct*. **11**, 395–412.

Stansby, P. K. 1976 The locking-on of vortex shedding due to the cross-stream vibration of circular cylinders in uniform and shear flows. *J. Fluid Mech*. **74**, 641–655.

Sumer, B. M. & Fredsøe, J. 1997 *Hydrodynamics around Cylindrical Structures*. World Scientific.

Techet, A. H., Hover, F. S. & Triantafyllou, M. S. 1998 Vortical patterns behind a tapered cylinder oscillating transversely to a uniform flow. *J. Fluid Mech*. **363**, 79–96.

Vickery, B. J. & Watkins, R. D. 1964 Flow-induced vibrations of cylindrical structures. In *Proc. First Australian Conf. on Hydraulics and Fluid Mechanics* (ed. R. Silvester). Pergamon.

Westerweel, J. 1993 *Digital Particle Image Velocimetry – Theory and Application*. Delft University Press.

Willert, C. E. & Gharib, M. 1991 Digital particle image velocimetry. *Exps. Fluids* **10**, 181–193.

Williamson, C. H. K. & Roshko, A. 1988 Vortex formation in the wake of an oscillating cylinder. *J. Fluids Struct*. **2**, 355–381.

Zdravkovich, M. M. 1982 Modification of vortex shedding in the synchronization range. *Trans. ASME*: *J. Fluids Engng* **104**, 513–517.

Zdravkovich, M. M. 1990 On origins of hysteretic responses of a circular cylinder induced by vortex shedding. *Z. Flugwiss. Weltraumforsch*. **14**, 47–58.